UNIVERSITÉ LAVAL

On the Modelization of Optical Devices

From Dielectric Cavities to Radiating Structures

Mémoire

Joey Dumont

Maîtrise en physique

Maître ès sciences (M.Sc.)

Québec, Canada

Résumé

Abstract

In recent years, outbursts in technology have changed the way we view, and do, science. In the days of yore, when the rose that is physics had not yet been given its name, science was in major part an experimental endeavour. It took the great Werner Heisenberg to establish theoretical physics as its own field. Today, however, it seems that the incredible ease with which we can produce data, throves upon throves of it, has spawned the idea that data is law, that data is self-suficient, that the throne of theory has been usurped by the opulent and almight data. In this thesis, we seek to reverse this trend by showing that theoretical analysis can yield physical insights inherently inaccessible to raw data.

We will first investigate the modelization of bidimensional dielectric cavities. The last decade has shown that this type of micron-sized device is ripe with applications ranging from biodetection to lasing action (more on that later). This has motivated the scientific community to investigate the behaviour of such cavities mostly as a function of their geometry, leaving their refractive index profile constant. We will generalize a scattering method that can deal with arbitrary geometry and arbitrary refractive index profiles and provides a way to accurately compute the resonances of such structures.

In the second part, we will discuss the modelization of radiating structures. Using the formalism developed in the previous section, we will study in detail the lasing properties of bidimensional cavities using the newly developed *self-consistent* ab initio *laser theory* (SALT). We will also attemt to model a class of antenna known as *leaky coax* antennas using a mix of semi-analytic and all-numerical methods. More specifically, we will attempt to explain the experimental data and the simulation data.

Table of Contents

List of Figures

List of Tables

Dedicated to a special collection of particles...

education, *n*. That which discloses to the wise and disguises from the foolish their lack of understanding.

The Devil's Dictionary
Ambrose Bierce

Notation

Mathematical Operators

Symbol	Definition
$\mathop{\mathrm{K}}_{m=1}^{\infty}\left(\frac{a_m}{b_m}\right)$	Continued fraction expansion with coefficients a_m and b_m.
$\sum_m$	Sum over all angular momenta in two dimensions, $m = -\infty \ldots \infty$.
$\sum_{\ell,m}$	Sum over all angular momenta in three dimensions, $\ell = 0 \ldots \infty$, $m = -\ell \ldots \ell$.
$\sum_{\sigma,\ell,m}$	Sum over all spinorial angular momenta in three dimensions.
$\lfloor x \rfloor$	Floor function. Maps x to the largest previous integer.
$\lceil x \rceil$	Ceiling function. Maps x to the smallest following integer.

Vectors and Matrices

Symbol	Definition
$\boldsymbol{V}$, $\boldsymbol{v}$	Vectors (bold and italic, uppercase and lowercase).
V_i, v_i	ith component of vector.
$\mathbf{M}$	Matrix (bold uppercase)
M_{ij}	Element on ith row and jth column. $(j + iN)$th element of matrix (row-major ordering) where N is the number of columns. The indices start at 0.

Electromagnetism

Symbol	Definition
$\boldsymbol{E}, \boldsymbol{D}, \boldsymbol{P}$	Electric field, electric displacement and polarization.
$\boldsymbol{H}, \boldsymbol{B}, \boldsymbol{M}$	Magnetic field, magnetic induction and magnetization.
$\boldsymbol{j}, \rho$	Current and charge densities.
$\boldsymbol{\chi}_{e,m}(\boldsymbol{r}, \boldsymbol{r}', t, t')$	Electric/magnetic tensorial susceptibility.
$\epsilon = \epsilon' + i\epsilon''$	Electric permittivity of a material. We often separate its real and imaginary parts as shown.
μ	Magnetic permeability of a material.
$n = \sqrt{\epsilon\mu}$	Refractive index of a material.
σ_e	Electric conductivity of a material.

Special Functions

Symbol	Definition
$J_\nu(z)$	Bessel function of the first kind of order ν.
$Y_\nu(z)$	Bessel function of the second kind of order ν.
$H_\nu^{(\pm)}(z)$, $H_\nu^{(\omega)}(z)$	Hankel functions of the first and second kind, respectively, of order ν, $\omega = \pm$.
$U(a, b, z)$	Kummer's function, also known as the confluent hypergeometric function of the first kind, with parameters a, b.

Angular Momentum

Ordering of angular momentum in 2D. We consider both positive and angular momentum, so the matrices have size $2M + 1 \times 2M + 1$ where M is the maximum angular momentum.

$$\mathbf{V}\boldsymbol{\psi} = \begin{array}{cc} & \begin{array}{ccc} & m' & \\ - & 0 & + \end{array} \\ m \begin{array}{c} - \\ 0 \\ + \end{array} & \begin{pmatrix} \ddots & & & & \iddots \\ & V_{-1-1} & V_{-10} & V_{-11} & \\ & V_{0-1} & V_{00} & V_{01} & \\ & V_{1-1} & V_{10} & V_{11} & \\ \iddots & & & & \ddots \end{pmatrix} \end{array} \begin{pmatrix} \vdots \\ \psi_{-1} \\ \psi_0 \\ \psi_1 \\ \vdots \end{pmatrix}$$

Ordering of angular momenta ℓ, m in 3D. This block structure allows the product

$$
\sum_{\ell'=0}^{\infty} \sum_{m'=-\ell'}^{\ell'} V_{\ell m, \ell' m'} \psi_{\ell' m'}
$$

to be written using a single index $\nu = (\ell, m)$. The matrices have size $(\ell_{\max}+1)^2 \times (\ell_{\max}+1)^2$.

$$
\mathbf{V}\boldsymbol{\psi} =
\begin{array}{cc}
 & \begin{array}{cccc} \overbrace{\qquad\qquad}^{\ell'=0} & \multicolumn{3}{c}{\overbrace{\qquad\qquad\qquad\qquad\qquad\qquad}^{m'=-\ell',\dots,\ell'}} \end{array} \\
\begin{array}{r} \ell = 0 \, \{ \\ \\ \ell = 1 \left\{ \vphantom{\begin{array}{c} V \\ V \\ V \end{array}} \right. \\ \\ \end{array}
&
\begin{pmatrix}
V_{00,00} & V_{00,1-1} & V_{00,10} & V_{00,11} \\
V_{1-1,00} & V_{1-1,1-1} & \vdots & \vdots \\
V_{10,00} & \cdots & \ddots & \vdots \\
V_{11,00} & \cdots & \cdots & \ddots
\end{pmatrix}
\end{array}
\begin{pmatrix}
\psi_{00} \\ \psi_{1-1} \\ \psi_{10} \\ \psi_{11} \\ \vdots
\end{pmatrix}
$$

Preface

Physics, maze, lost in a maze, partial results

Chapter 1

Introduction

Our story begins, as most stories do, with a simple premise. Circa 1878, John William Strutt, Third Baron Rayleigh – Lord Rayleigh, for short – observed a peculiar phenomena in St Paul's Cathedral: a small whisper, uttered from one side of the circular gallery, could be heard quite clearly by anyone seated along the outer edge of the gallery and even travel back to the ears of the whisperer. To explain his observation, Lord Rayleigh borrowed from geometrical optics and modelled the sound waves as packets, or particles, of sound that undergo specular reflection upon contact with an obstacle [1, §287]. This picture, akin to the trajectories of billiard balls, allowed him to conclude that "sonorous vibrations have a tendency to cling to a concave surface". The billiard analysis is later complemented by a complete wave analysis wherein he shows that the equation of aerial vibrations, essentially Helmholtz's equation, admit solutions of the form

$$\psi_n(r,\theta,t) = J_n(kr)\cos(kat - n\theta)$$

and that most of the amplitude, for a certain range of parameters, is concentrated in an annulus near the boundary of the gallery [2], further proving his explanation. He also noted that his derivation held for electrical waves if the walls were perfectly conducting. He termed this phenomena the whispering-gallery phenomena and, today, we call this type of waves whispering-gallery waves.

Our story thus begins with the endless voyage of a whisper along a concave surface and all the secrets it may or may not convey...

1.1 The Study of Passive Dielectric Microcavities

For the better part of the 20$^{\text{th}}$ century, the whispering-gallery phenomena remained only a matter of curiosity [3]. It was brought back to light in the mid-1980s when it was realized that *dielectric resonators* had the potential to attain unparalleled electromagnetic energy storage capabilities via the use of whispering-gallery waves [4]. Research in this area exploded when their application

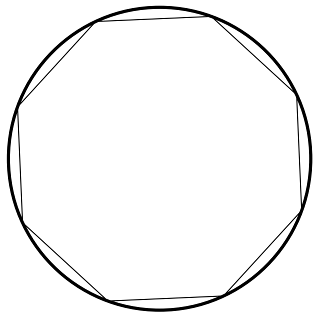

(a) Closed cavity with a WGM of quantum number $m = 8$.

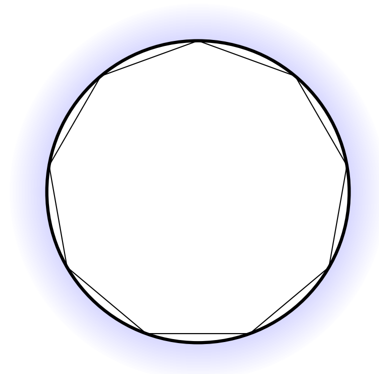

(b) Open cavity with a WGM of quantum number $m = 9$.

Figure 1.1 – Schematic representation of whispering-gallery modes in closed and open resonators. In closed resonators, WGMs have infinite lifetimes as they cannot interact with the external world. In open cavities, evanescent leakage (represented by the blue glow), implies finite modal lifetime.

as extremely sensitive biosensors was theoretically explored and later experimentally achieved [5–8].

The whispering-gallery phenomena in dielectric media can be explained via the same basic physics as the whispering gallery of St Paul's Cathedral, but with a crucial difference: the mechanism by which the light (or sound) is confined. Both the cathedral and the metallic sphere described by Lord Rayleigh as known as *closed cavities*: the whisper does not leave the interior of the gallery as the electric field does not leave the confines of its metallic prison. The walls of the cavity do not allow the waves to penetrate their depth. On the other hand, dielectric cavities retain light by way of *total internal reflection*, which allows the wave to leak, or couple, to the exterior of the cavity. This has a slew of experimental and theoretical consequences.

Mathematically, closed cavities usually obey Helmholtz's equation

$$\left[\nabla^2 + k^2\right]\psi = 0 \qquad \psi(\boldsymbol{r} \in \mathscr{C}) = 0 \tag{1.1}$$

where ψ is the oscillation (pressure field, electric field, etc.) and $\mathscr{C}$ is the boundary of the cavity. This partial differential equation together with the Dirichlet boundary condition translates to an eigenvalue problem: solutions only exist for a discrete set of eigenvalues k_n. These closed cavities have been a testbed for theoretical and experimental endeavours in the last three decades, as can be seen from the great amount of work done in the fields of quantum chaos and random matrix theory (RMT), for instance. Quantum chaos attempts to classify the chaotic eigenstates of systems with non-separable Schrödinger equations using the underlying (semi)classical mechanics of the cavity. Research in this area helps to define the classical-quantum transition. Level-spacing statistics of closed cavities also provides a way to classify the eigenstates, depending on the statistical ensemble the cavity describes.

Close cavities, are, however, an idealization of the much more realistic open cavity. The discrete states of the former exist indefinitely inside the cavity; they have an infinite lifetime. They thus have infinite energy storage capabilities, but are impossible to generate. The latter, which also obey Helmholtz equation, but with the Sommerfeld radiation condition (a Robin boundary condition)

$$\lim_{r\to\infty} r^{\frac{d-1}{2}} \left(\frac{\partial}{\partial r} - ik\right)\psi = 0 \tag{1.2}$$

have a continuum of solutions. These solutions have finite lifetimes. An incoming field from infinity can interact with the modes of the cavity and escape the confines of the cavity. The *time delay* introduced by the interaction is linked to the lifetime of the modes of the cavity.

This rather pictorial viewpoint can be made formal by the use of *scattering theory*, in which we suppose that a field, coming from infinity, suffers some changes due to its interaction with the cavity and espaces to infinity once again. The object that we will consider is the scattering matrix, which describes the relationship between the field after the interaction to the field before the interaction, i.e. it describes the effect of the potential on an incoming field. The scattering approach allows us to define the modes of open cavities, a problem that is perhaps more complicated that it seems (Fox-Li modes, modes of wave-chaotic...).

Discuss resonances and Q values.

Open dielectric cavities also allow a semiclassical approximation, mathematically obtained by letting the wavelength λ to be very small compared to the characteristic lengths involved in the system, or $k \to \infty$. The resulting open billiard can and has been used to engineer the cavities to specific purposes . The fact that the resulting system is Hamiltonian (but not necessarily Hermitian) has been used to study open quantum systems and non-Hermitian quantum mechanics experimentally. This stems from the similarities between the Helmholtz and Schrödinger equations.

Discuss CAT, biosensing, microlasers...

Most applications of open dielectric cavities urge the use of very high Q resonances. In WGM biosensors, the Q value dictates the performance of the sensor; in microlasers, it means a better field enhancement; in cavity QED, higher Q and lower mode volumes make it possible to study the quantum effects of light-matter interaction. It is possible to experimentally obtain values of $Q \sim 10^7 - 10^9$ using highly symmetrical cavity designs. This symmetry implies that the far-field emission is also symmetry: it usually is isotropic. For some applications, such as some designs of WGM biosensors, this may be fine. However, for lasing applications, one would like to have, simultaneously, high-Q and directionality in the far-field emission. The duality of those two concepts is one of the many facets of the study of asymmetric resonant cavities (ARCs), dielectric cavities that are parametrically deformed versions of the circular cavity. This allows a certain degree of freedom in the design of microcavities and has lead to interesting phenomena, such as ...

Add references.

add references.

In this thesis, we will a second degree of freedom in the design by allowing the refractive index distribution to be completely arbitrary inside the cavity. This new degree of freedom can be realized experimentally by the use of nematics. Moreover, we will see that the numerical methods developed in this context could also be used to better model the lasing operation of active dielectric cavities.

1.2 Onwards to Radiating Structures

The expertise developed in the study of dielectric cavities was later extended to lasing cavities and proposed for arbitrary 3D structures. We will touch upon the modelization of active dielectric cavities with the use of steady-state *ab initio* laser theory (SALT) which, as its name hints, provides a steady-state model for the behaviour of the active medium. The particular set of approximations used allow to model the population dynamics of quantum N-level systems as a static, but possibly spatially-varying and non-linear, modification of the refractive index of the passive cavity. In the linear case, basis expansions methods (such as the ones we use) can be applied. We will consider another numerical approach that has the potential to better compute the interior field, the variable phase method.

We will also discuss the application of the method to arbitrary 3D structures. We will attempt to model a type of antennae called leaky coax antenna (LCX). Their highly non-trivial geometry and the specifics of their experimental realization will make our method rather hard to implement in that case. We will thus use all-numerical methods to extract the necessary information. Proper introduction to this project will be given later.

1.3 Content of this Work

In first chapter of this thesis, we detail our work on open dielectric cavities with arbitrary refractive index profiles. We generalize a scattering method by G.P.-A. [9] for complex refractive indices and TE polarization. We first describe the analytical formalism and develop some of the scattering theory that is needed. We then discuss the development and numerical implementation of the solution of Helmholtz's equation in inhogemeneous cavities. We then showcase the method by analyzing a circular microcavity with a Gaussian deformation of its refractive index.

The second chapter discuss the extension to lasing structures and briefly discusses the variable phase method. We then model a family of LCXs with the finite element method (FEM). Most of the work done aimed to reconciliate the experimental and theoretical data sets, mainly by explaining the source of the discrepancy. The effects of several physical parameters were thus explored.

Chapter 2

Passive Media

This chapter is devoted to the study of light propagation in dielectric bidimensional cavities. Starting from Maxwell's equations, we derive approximate differential equations that govern the wave behaviour in cavities having spatially-varying refractive index profiles (henceforth referred to as *inhomogeneous cavities*). This set of reduced equations serves as the basis for a semi-analytical solution method that uses the quantum machinery of the **S**-matrix and its associated time-delay matrix to yield information about the cavity modes. The numerical implementation of the method is discussed and and is then demonstrated for a selected set of microcavities.

2.1 Maxwell's Equations for Bidimensional Cavities: Reduction from 3D to 2D

2.1.1 Setting the Stage

As with any problem in optics, we start from Maxwell's equations. Although this specific chapter focuses on dielectric cavities, we will show Maxwell's equations in their full generality, as we will later study problems with currents and sources. We use the Lorentz-Heaviside set of units with the speed of light, c, equal to 1.

$$\nabla \times \boldsymbol{E}(\boldsymbol{r},t) + \frac{\partial \boldsymbol{B}(\boldsymbol{r},t)}{\partial t} = 0 \tag{2.1a}$$

$$\nabla \times \boldsymbol{H}(\boldsymbol{r},t) - \frac{\partial \boldsymbol{D}(\boldsymbol{r},t)}{\partial t} = \boldsymbol{j}_s(\boldsymbol{r},t) + \boldsymbol{j}_c(\boldsymbol{r},t) \tag{2.1b}$$

$$\nabla \cdot \boldsymbol{D}(\boldsymbol{r},t) = \rho(\boldsymbol{r},t) \tag{2.1c}$$

$$\nabla \cdot \boldsymbol{B}(\boldsymbol{r},t) = 0 \tag{2.1d}$$

where $\boldsymbol{E}$ is the electric field, $\boldsymbol{D}$ the electric displacement, $\boldsymbol{H}$ the magnetic field, $\boldsymbol{B}$ the magnetic induction and where $\boldsymbol{j}$ and ρ are the current and charge densities, respectively. The distinction between a source current, $\boldsymbol{j}_s$ and an induced conduction current, $\boldsymbol{j}_c$, is arbitrary but will prove conceptually useful when dealing with radiating structures (see next chapter). In this thesis, we will generally take $\rho = 0$ and $\boldsymbol{j}_s = \boldsymbol{0}$ as there will be no physical charges/currents in our problems.

This very general set of equations does not make any assumption on the properties of the medium in which the fields exist: it is, therefore, almost impossible to solve. To properly model the effect of different media, we introduce the usual constitutive relations:

$$\boldsymbol{D}(\boldsymbol{r},t) = \boldsymbol{E}(\boldsymbol{r},t) + \boldsymbol{P}(\boldsymbol{r},t) \tag{2.2a}$$

$$\boldsymbol{B}(\boldsymbol{r},t) = \boldsymbol{H}(\boldsymbol{r},t) + \boldsymbol{M}(\boldsymbol{r},t) \tag{2.2b}$$

where the effects of the medium are accounted for in $\boldsymbol{P}$ and $\boldsymbol{M}$, the polarization and magnetization fields, respectively. In the time domain, the effect of the electric (magnetic) field on the polarization (magnetization) can be written as

$$\boldsymbol{P} = \iiiint \boldsymbol{\chi}_e(\boldsymbol{r},\boldsymbol{r}',t,t';\boldsymbol{E}) \cdot \boldsymbol{E}(\boldsymbol{r}',t') d^3\boldsymbol{r}' dt' + \boldsymbol{P}^{NL} \tag{2.3a}$$

$$\boldsymbol{j}_c = \iiiint \boldsymbol{\sigma}_e(\boldsymbol{r},\boldsymbol{r}',t,t';\boldsymbol{E}) \cdot \boldsymbol{E}(\boldsymbol{r}',t') d^3\boldsymbol{r}' dt' + \boldsymbol{j}_c^{NL} \tag{2.3b}$$

$$\boldsymbol{M} = \iiiint \boldsymbol{\chi}_m(\boldsymbol{r},\boldsymbol{r}',t,t';\boldsymbol{H}) \cdot \boldsymbol{H}(\boldsymbol{r}',t') d^3\boldsymbol{r}' dt' + \boldsymbol{M}^{NL} \tag{2.3c}$$

where $\boldsymbol{\chi}_{e,m}$ are the electric and magnetic tensorial susceptibilities and $\boldsymbol{\sigma}_e$ the tensorial electric conductivity. They are written here as (possibly non-linear) response functions. We will take the nonlinear magnetization and induced current, $\boldsymbol{M}^{NL}$ and $\boldsymbol{j}_c^{NL}$, to be identically zero. While $\boldsymbol{P}^{NL}$ is usually reserved for the nonlinear polarization, we will use it to denote the effect of a gain medium, whether it is nonlinear or not.

While it is possible to compute these quantities from first principles using statistical mechanics techniques, this is a highly complicated topic that we will not delve into. We will consider local, causal and isotropic (although possibly spatially varying) responses. The tensorial response functions become scalar and their spatial dependence is given by a three dimensional Dirac δ-function. This allows us to write the constitutive relations in the much simpler form

$$\boldsymbol{P} = \int_0^\infty \chi_e(\boldsymbol{r},t')\boldsymbol{E}(\boldsymbol{r},t-t')dt' + \boldsymbol{P}^{NL} \tag{2.4a}$$

$$\boldsymbol{j}_c = \int_0^\infty \sigma_e(\boldsymbol{r},t')\boldsymbol{E}(\boldsymbol{r},t-t')dt' \tag{2.4b}$$

$$\boldsymbol{M} = \int_0^\infty \chi_m(\boldsymbol{r},t')\boldsymbol{H}(\boldsymbol{r},t-t')dt' \tag{2.4c}$$

Substituting these results into the Maxwell equations and and using the Fourier transform yields

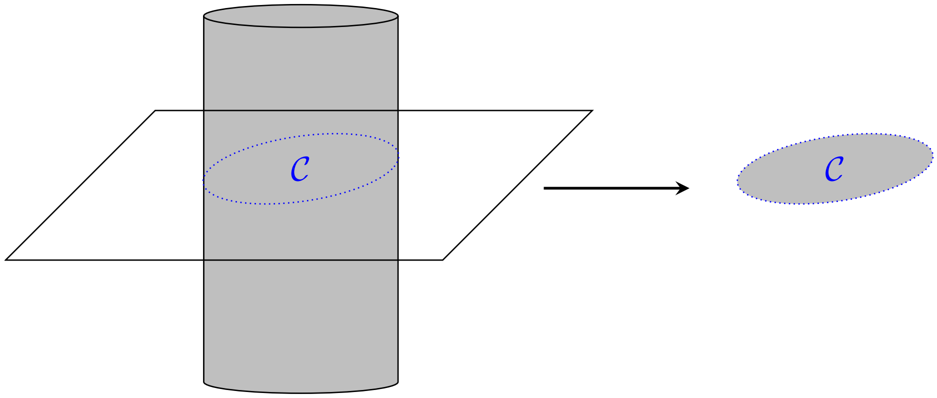

Figure 2.1 – Our set of equations will be valid for infinitely long cylinders of arbitrary cross-sections (shown on the left) and arbitrary physical parameters ϵ and μ. Our cavities, however, are bidimensional (shown on the right). The dimension reduction thus consists in postulating independence of the fields and physical and geometrical parameters of the cavity with regards to the longitudinal coordinate and choosing a particular plane $\partial\Omega$.

the set [1]

$$\nabla \times \boldsymbol{E}(\boldsymbol{r},\omega) - i\omega\mu(\boldsymbol{r},\omega)\boldsymbol{H}(\boldsymbol{r},\omega) = 0 \tag{2.5a}$$

$$\nabla \times \boldsymbol{H}(\boldsymbol{r},\omega) + i\omega\epsilon(\boldsymbol{r},\omega)\boldsymbol{E}(\boldsymbol{r},\omega) = -i\omega\boldsymbol{P}^{NL}(\boldsymbol{r},\omega) \tag{2.5b}$$

where $\mu = 1 + \chi_m$ is the permeability and $\epsilon = 1 + \chi_e - \sigma/i\omega$ the permittivity. In the remainder of this thesis, we will concerned by the solution of this precise set of equations. We also recall the *electromagnetic boundary conditions* associated with a discontinuous jump in the permeability or permittivity

$$\hat{\boldsymbol{n}} \cdot (\boldsymbol{B}_2 - \boldsymbol{B}_1) = 0, \qquad \hat{\boldsymbol{n}} \times (\boldsymbol{E}_2 - \boldsymbol{E}_1) = 0, \tag{2.5c}$$

$$\hat{\boldsymbol{n}} \times (\boldsymbol{H}_2 - \boldsymbol{H}_1) = \boldsymbol{K}, \qquad \hat{\boldsymbol{n}} \cdot (\boldsymbol{D}_2 - \boldsymbol{D}_1) = \Sigma. \tag{2.5d}$$

2.1.2 Dimension Reduction

In this section we derive the differential equations for the electromagnetic field in an infinitely long dielectric cylinder of arbitrary cross-section and arbitrary physical parameters ϵ and μ. There is no gain medium. Consequently, $\boldsymbol{P}^{NL} = \boldsymbol{K} = \Sigma \equiv 0$ in our previous equations. We also require translational symmetry, i.e. that there exist no parametric dependence on z.

To this effect, it will be useful to separate the field in tranverse and longitudinal components. Following [10, 11], we suppose the fields can be written as

$$\begin{Bmatrix} \boldsymbol{E}(\boldsymbol{r}_\perp, z) \\ \boldsymbol{H}(\boldsymbol{r}_\perp, z) \end{Bmatrix} = \begin{Bmatrix} \boldsymbol{E}(\boldsymbol{r}_\perp) \\ \boldsymbol{H}(\boldsymbol{r}_\perp) \end{Bmatrix} e^{i\beta z} \tag{2.6}$$

[1]Notice that, in our system of units, $\omega = k$ and thus we will make use of frequency and wavenumber interchangeably. We will also suppress all explicit frequency dependence from our notation, as it rapidly becomes cumbersome.

and we will also separate the fields and differential operators in two parts

$$\boldsymbol{E}(\boldsymbol{r}_\perp) = \boldsymbol{E}_\perp + E_z\hat{\boldsymbol{z}}; \qquad \nabla = \nabla_\perp + \hat{\boldsymbol{z}}\frac{d}{dz}. \tag{2.7}$$

Substitution in (2.5a) yields

$$ik\mu H_z = (\nabla_\perp \times \boldsymbol{E}_\perp)_z \qquad -ik\epsilon E_z = (\nabla_\perp \times \boldsymbol{H}_\perp)_z \tag{2.8}$$

$$ik\mu \boldsymbol{H}_\perp = (-i\beta\boldsymbol{E}_\perp + \nabla_\perp E_z)\times\hat{\boldsymbol{z}} \qquad -ik\epsilon\boldsymbol{E}_\perp = (-i\beta\boldsymbol{H}_\perp + \nabla_\perp H_z)\times\hat{\boldsymbol{z}} \tag{2.9}$$

The symmetry of these equations allow the decoupling of the tranverse and longitudinal components. Solving the system (2.9) shows that the scalar components H_z and E_z are the fundamental ones:

$$\boldsymbol{E}_\perp = \frac{i}{k^2n^2-\beta^2}\left[\beta\nabla_\perp E_z + k\mu\nabla_\perp H_z\times\hat{\boldsymbol{z}}\right] \tag{2.10a}$$

$$\boldsymbol{H}_\perp = \frac{i}{k^2n^2-\beta^2}\left[-k\epsilon\nabla_\perp E_z\times\hat{\boldsymbol{z}} + \beta\nabla_\perp H_z\right]. \tag{2.10b}$$

Derivation of the differential equation for E_z and H_z can be done via equations (2.8), but is quite cumbersome. A component-wise approach is thus presented in Appendix B.

More specific boundary conditions can be derived with the use of these equations. Applying the tranverse and longitudinal decomposition on (2.5c) yields the six boundary conditions

$$\begin{aligned} E_{z1} &= E_{z2} & H_{z1} &= H_{z2} \\ E_{t1} &= E_{t2} & H_{t1} &= H_{t2} \\ \epsilon_1 E_{n1} &= \epsilon_2 E_{n2} & \mu_1 H_{n1} &= \mu_2 H_{n2} \end{aligned}$$

We seek to write the boundary conditions as a function of H_z and E_z, given that they are the fundamental fields. This can be done by taking the projections of the tranverse fields:

$$E_t = \hat{\boldsymbol{t}}\cdot\boldsymbol{E}_\perp = \frac{i}{\gamma^2}\left[\beta\partial_t E_z - k\mu\partial_n H_z\right] \tag{2.11a}$$

$$E_n = \hat{\boldsymbol{n}}\cdot\boldsymbol{E}_\perp = \frac{i}{\gamma^2}\left[\beta\partial_n E_z + k\mu\partial_t H_z\right] \tag{2.11b}$$

$$H_t = \hat{\boldsymbol{t}}\cdot\boldsymbol{H}_\perp = \frac{i}{\gamma^2}\left[k\epsilon\partial_n E_z + \beta\partial_t H_z\right] \tag{2.11c}$$

$$H_n = \hat{\boldsymbol{n}}\cdot\boldsymbol{H}_\perp = \frac{i}{\gamma^2}\left[-k\epsilon\partial_t E_z + \beta\partial_n H_z\right] \tag{2.11d}$$

where $\partial_{t,n}$ are the tranverse and normal derivatives, respectively, and $\gamma^2 = k^2n^2 - \beta^2$. Substituting these results in the boundary conditions for the tranverse and normal components, we can derive the conditions $\partial_t E_{z1} = \partial_t E_{z2}$, $\partial_t H_{z1} = \partial_t H_{z2}$, which can shown to be equivalent to the continuity of the longitudinal components, *viz.* (2.11a) [11]. Combining all our previous results yields the four independent boundary conditions:

$$E_{z1} = E_{z2} \tag{2.12a}$$

$$H_{z1} = H_{z2} \tag{2.12b}$$

$$\frac{k\mu_1}{\gamma_1^2}\frac{\partial H_{z1}}{\partial n} - \frac{k\mu_2}{\gamma_2^2}\frac{\partial H_{z2}}{\partial n} = \beta\left(\frac{1}{\gamma_1^2} - \frac{1}{\gamma_2^2}\right)\frac{\partial E_{z1}}{\partial t} \tag{2.12c}$$

$$\frac{k\epsilon_1}{\gamma_1^2}\frac{\partial E_{z1}}{\partial n} - \frac{k\epsilon_2}{\gamma_2^2}\frac{\partial E_{z2}}{\partial n} = -\beta\left(\frac{1}{\gamma_1^2} - \frac{1}{\gamma_2^2}\right)\frac{\partial H_{z1}}{\partial t}. \tag{2.12d}$$

Notice that the propagation constant couples the electric and magnetic field, regardless of the physical and geometrical parameters of the cavity.

2.2 Scattering Matrix Formalism

The previous section has provided us with the differential equations that we will need to solve to properly model bidimensional cavities. In this section, we will set up a scattering matrix (**S**-matrix) formalism, augmented by the **Q**-*matrix* that will allow us to quantify the response of the cavities to an applied field and provide us with a novel way to determine their resonances. The numerical implementation of the method, being somewhat problematic, will be discussed at length.

2.2.1 **S** and **Q** Matrices Reloaded

In dielectic cavities, we need to solve the following equations

$$\begin{aligned}\left\{\nabla^2 + k^2 n^2\left[1 - \left(\frac{\beta}{kn}\right)^2\right]\right\}\begin{Bmatrix} H_z \\ E_z \end{Bmatrix} &= \frac{1}{1-\left(\frac{\beta}{kn}\right)^2}\left[\frac{1}{\epsilon}\begin{Bmatrix}\nabla H_z \\ \nabla E_z\end{Bmatrix}\cdot\nabla\epsilon + \frac{1}{\mu}\begin{Bmatrix}\nabla H_z \\ \nabla E_z\end{Bmatrix}\cdot\nabla\mu\right] \\ &-\begin{pmatrix}\frac{1}{\mu} & 0 \\ 0 & \frac{1}{\epsilon}\end{pmatrix}\begin{Bmatrix}\nabla H_z\cdot\nabla\mu \\ \nabla E_z\cdot\nabla\epsilon\end{Bmatrix} + \frac{\beta/kn}{1-\left(\frac{\beta}{kn}\right)^2}\left[\left(\sqrt{\frac{\mu}{\epsilon}} + \sqrt{\frac{\epsilon}{\mu}}\right)\begin{pmatrix}0 & -\frac{1}{\mu} \\ \frac{1}{\epsilon} & 0\end{pmatrix}\begin{Bmatrix}\nabla H_z \times \nabla\mu \\ \nabla E_z \times \nabla\epsilon\end{Bmatrix}\right]\end{aligned} \tag{2.13}$$

where β is the propagation constant in the longitudinal direction. Inhomogeneous cavities do not obey Helmholtz's equation like homogeneous cavities do, but depend upon the first-order derivatives of the fields and physical properties of the medium. The two longitudinal fields couple through the last term, where an antidiagonal matrix appears.

In fact, this set of equations describe the propagation of light in optical fibers of arbitrary cross-section and arbitrary refractive index profiles. However, we are interested in the modes that are confined on a two-dimensional surface, the cavity modes. These modes must be independent of z and we therefore take $\beta = 0$. This is the main approximation of our model. It has been shown to hold only approximately in experimental conditions [12, 13], but we take the resulting equations to be the exact one. This allow a simpler analysis for qualitative exploration; quantitative agreement could be reached via perturbation methods. This approximation has the much appreciated benefit of decoupling both the field equations and the boundary conditions (see (2.12)).

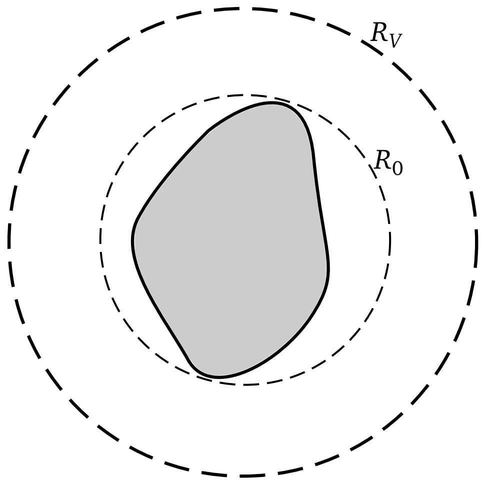

Figure 2.2 – Geometry of a dimensional cavity. R_0 is the radius of the smallest circle that encloses the physical microcavity. R_V is the radius of a fictional circle that we will take to go to infinity.

Additionnally exploiting the fact that we will only consider non-magnetic media ($\mu = 1$, $\epsilon = n^2$), our equation set becomes

$$\left[\nabla^2 + k^2 n^2\right] H_z = \frac{2}{n} \nabla H_z \cdot \nabla n \tag{2.14a}$$

$$\left[\nabla^2 + k^2 n^2\right] E_z = 0. \tag{2.14b}$$

In the following, it will be advantageous to form the field $\boldsymbol{h} = \boldsymbol{H}/n$ [14]. This yields the equation [9, 14]

$$\left[\nabla^2 + k^2 n^2 - \frac{2(\nabla n)^2}{n^2} + \frac{\left(\nabla^2 n\right)}{n}\right] h_z = 0 \tag{2.14a'}$$

which is nothing but Helmholtz equation with an additional potential term.

To solve these equations, we will adopt a scattering viewpoint. Imagine that the dielectric cavity is embedded in an infinite medium of constant refractive index $n_o = \sqrt{\epsilon\mu}$, outside the cavity, $\boldsymbol{r} \notin \mathscr{C}$, the r.h.s. of our set vanishes. The resulting equations are Helmholtz's and therefore have the well-known solution

$$\psi = \sum_m \left[A_m H_m^{(-)}(nkr) + B_m H_m^{(+)}(nkr)\right] e^{im\theta} \qquad (r > R_0). \tag{2.15}$$

where $H_m^{(\pm)}(z)$ are the Hankel functions of the first and second kind. The Hankel functions are chosen in lieu of their usual homologues $J_m(z)$ and $Y_m(z)$ as their asymptotic forms have incoming/outgoing cylindrical wave character, $H_m^{(\pm)} \propto \exp(\pm ikr)/\sqrt{r}$. The scattering viewpoint essentially describes the relationship between the outgoing coefficients, B_m, and the incoming coefficients, A_m via the *scattering matrix*

$$B_m = S_{mm'} A_{m'}. \tag{2.16}$$

Much like its quantum-mechanical counterpart, the scattering matrix can be interpreted as a phase shift acquired by the incoming waves through interaction with the potential. This is most easily seen by considering a central potential $V(r)$ where the $\mathbf{S}$-matrix is diagonal. In that case, the m component of the field can be written as

$$\psi_m \propto \frac{1}{\sqrt{r}}\left[e^{-ikr} + e^{i\delta_m}e^{ikr}\right] \tag{2.17}$$

where we have written $S_{mm} = e^{i\delta_m}$ with $\delta_m \in \mathbb{R}$ as per the unitarity condition. The non-diagonal generalization $S_{mm'}$ describes the coupling between angular momenta $m \to m'$ and can be interpreted as a transition probability. It should be noted that the $\mathbf{S}$-matrix contains all near- and far-field information.

In most applications, we wish to find the *resonances* of the cavity. This is usually done by enforcing Sommerfeld radiation conditions on Helmholtz's equation and looking for solutions of

link to introduction

$$\mathbf{S}^{-1}\boldsymbol{B} = 0; \tag{2.18}$$

i.e. an infinitesimal input provides an infinite output. A solution exists only if $|\det \mathbf{S}(k)| \to \infty$, at a pole of the $\mathbf{S}$-matrix. For real potentials, there cannot exist a solution on the real k line because of the flux conservation (unitarity) property of the $\mathbf{S}$-matrix. We must extend the search to the complex k plane.

Non-renormalizable QB states.

Complex potentials -> trajectory of poles in k plane to real line. Freddy foreshadowing for next part.

We will proceed a different way. It is possible to find the signatures of these poles on the real k line by computing the *energy* of the modes and their complex coupling. This part of the formalism was initally developed by G.P.-A. [9]: we will repeat only what is necessary.

Recall that the average electromagnetic energy of a field in a given volume V

$$\mathscr{E}^V = \frac{1}{2}\iiint_V \left[\epsilon \boldsymbol{E}^* \cdot \boldsymbol{E} + \mu \boldsymbol{H}^* \cdot \boldsymbol{H}\right] d^3\boldsymbol{r}. \tag{2.19}$$

We form the energy matrix

$$\mathscr{E}^V_{mm'} = \frac{1}{2}\iiint_V \left[\epsilon \boldsymbol{E}^*_m \cdot \boldsymbol{E}_{m'} + \mu \boldsymbol{H}^*_m \cdot \boldsymbol{H}_{m'}\right] d^3\boldsymbol{r}. \tag{2.20}$$

We will carry out the rest of the computation for the TM mode ($H_z = E_r = E_\theta = 0$); the argument holds for TE polariation *mutatis mutandis* because of the k-independence of the additional potential term in (2.14a') and also because $\boldsymbol{h} \propto \boldsymbol{H}$ for $r > R_0$. We thus have

$$\boldsymbol{E} = \psi \hat{\boldsymbol{z}}$$
$$\boldsymbol{H} = \frac{1}{ik} \nabla \times \boldsymbol{E}$$

and the energy matrix becomes

$$\mathscr{E}^V_{mm'} = \frac{1}{2} \iiint_V \left[\epsilon \psi^*_m \psi_{m'} + \frac{1}{k^2} (\nabla \times \psi_m \hat{\boldsymbol{z}}) \cdot \left(\nabla \times \psi^*_{m'} \hat{\boldsymbol{z}} \right) \right] d^3\boldsymbol{r}. \tag{2.21}$$

Taking the parametric derivative of Helmholtz' equation, we get the following relations

$$\left[\nabla^2 + n^2 k^2 \right] \psi = 0 \tag{2.22a}$$
$$\left[\nabla^2 + n^2 k^2 \right] \psi^* = 0 \tag{2.22b}$$
$$\nabla^2 \frac{\partial \psi}{\partial k} + 2kn^2 \psi + n^2 k^2 \frac{\partial \psi}{\partial k} = 0 \tag{2.22c}$$

where we assume a real potential. Forming the product

$$\begin{aligned} \frac{1}{2k} \nabla \cdot \left[\frac{\partial \psi}{\partial k} \nabla \psi^* - \psi^* \nabla \frac{\partial \psi}{\partial k} \right] &= \frac{1}{2k} \left[\nabla \psi^* \cdot \nabla \frac{\partial \psi}{\partial k} + \frac{\partial \psi}{\partial k} \nabla^2 \psi^* - \nabla \frac{\partial \psi}{\partial k} \cdot \nabla \psi^* - \psi^* \nabla^2 \frac{\partial \psi}{\partial k} \right] \\ &= \frac{1}{2k} \left[n^2 \psi^* \left(2k\psi + k^2 \frac{\partial \psi}{\partial k} \right) - \frac{\partial \psi}{\partial k} n^2 k^2 \psi^* \right] \\ &= n^2 \psi^* \psi \end{aligned}$$

where we have used the identity [15, Appendix II]

$$\nabla \cdot (\phi \boldsymbol{A}) = \boldsymbol{A} \cdot \nabla \phi + \phi \nabla \cdot \boldsymbol{A}. \tag{2.23}$$

We will also use the identity

$$(\boldsymbol{a} \times \boldsymbol{b}) \cdot (\boldsymbol{c} \times \boldsymbol{d}) = \boldsymbol{a} \cdot [\boldsymbol{b} \times (\boldsymbol{c} \times \boldsymbol{d})] \tag{2.24}$$

to write the energy matrix as

$$\mathscr{E}^V_{mm'} = \frac{1}{4k} \int_V \nabla \cdot \left\{ \frac{\partial \psi_{m'}}{\partial k} \nabla \psi^*_m - \psi^*_m \nabla \frac{\partial \psi_{m'}}{\partial k} + \frac{2}{k} \left[\psi_{m'} \hat{\boldsymbol{z}} \times \nabla \times \psi^*_m \hat{\boldsymbol{z}} \right] \right\} d^3\boldsymbol{r} \tag{2.25}$$

Using the divergence theorem, noting that the normal vector is the radial vector, we obtain

$$\mathscr{E}^V_{mm'} = \frac{wR_V}{4k} \int_0^{2\pi} \left(\frac{\partial \psi_{m'}}{\partial k} \frac{\partial \psi^*_m}{\partial r} - \psi^*_m \frac{\partial^2 \psi_{m'}}{\partial k \partial r} \right) d\theta + \frac{wR_V}{2k} \int_0^{2\pi} \psi_{m'} \frac{\partial \psi^*_m}{\partial r} d\theta$$

Using the exterior solution for ψ_m and using the asymptotic expressions (A.16c) for the Hankel functions, we get (after some algebra)

$$\mathscr{E}^\infty_{mm'} = \lim_{R_V \to \infty} \left[\frac{4n_0 w R_V}{k} + \mathscr{O}(R_V^{-1}) \right] \delta_{mm'} + \frac{4w}{k} \left(-i \sum_\ell S^*_{\ell m} \frac{\partial S_{\ell m'}}{\partial k} \right) \tag{2.26}$$

where w is the thickness of the cavity. The first term is the diverging energy of the beam. Given that the incoming and outgoing waves are of infinite extent, this divergence is only natural. The second term, however, depends only the potential and can be interpreted as an excess energy due to the cavity [9]. In matrix notation, we have

$$\mathbf{Q} = -i\mathbf{S}^{\dagger}\frac{d\mathbf{S}}{dk}. \tag{2.27}$$

This result coincides with the **Q**-matrix of quantum mechanics [16]. The interpretation of this matrix is facilited by (2.17). Using the central potential, we can write

$$Q_{mm} = -ie^{-i\delta_m}\left(i\frac{\partial\delta_m}{\partial k}\right)e^{i\delta_m} = \frac{\partial\delta_m}{\partial k}. \tag{2.28}$$

The **Q**-matrix thus corresponds to the energy derivative of the phase shift, which has long been associated with the time-delay introduced by the potential [16–18].

The keen reader will have noticed that the above derivation fails for complex potentials. The author has not found a proper derivation for the extension to complex potentials. However, an expression can be found by this heuristic argument: when the potential is complex, the phase shift δ_m becomes a complex function of k. In the preceding expression, we should take the inverse of the scattering matrix, not its Hermitian transpose, to reproduce the energy derivative of the phase shift. We thus have

$$\mathbf{Q} = -i\mathbf{S}^{-1}\frac{\partial\mathbf{S}}{dk} \tag{2.29}$$

as the proper generalization. This form was also used by Smith in [16].

2.2.2 Properties of the S and Q matrices

The **S**-matrix has multiple symmetries which can be used either to verify numerical implementations or to help tame numerical divergence issues. Most of the symmetries we will expose in this thesis will concern the analytical continuation of the scattering matrix in the complex k plane.

It is well known that the **S**-matrix is unitary for real values of n and k [19]. However, it loses this important property is lost when we extend to the complex plane. Looking at the complex conjugated versions of our equation set, we see that we have

$$\begin{aligned} B_m &= S_{mm'}(n,k)A_{m'} \\ A_m^* &= S_{mm'}(n^*,k^*)B_{m'}^* \end{aligned}$$

we can obtain the relation

$$\mathbf{S}^{-1}(n^*,k^*) = \mathbf{S}^{\dagger}(n,k) \tag{2.30}$$

which reduces to the unitarity condition when the values are real.

Following [9], we set up the following scattering "experiment":

$$H_m^{(-)}(z)e^{im\theta} \to \sum_{m'} S_{m'm}(n,k)H_{m'}^{(+)}(z)e^{im'\theta} \qquad \text{(initial reaction)}$$

$$\sum_m S^*_{m'm}(n^*,k^*)H_m^{(-)}(z)e^{im\theta} \to H_{m'}^{(+)}(z)e^{im'\theta} \qquad \text{(relation (2.30))}$$

$$\sum_m S_{m'm}(n^*,k^*)\overline{H_m^{(-)}(z)}e^{-im\theta} \leftarrow \overline{H_{m'}^{(+)}(z)}e^{-im'\theta}. \qquad \text{(complex conjugate (time reversal))}$$

Use of (A.8c) leads to the relation, valid only when $k \in \mathbb{R}$

$$S_{m'm}(n,k) = (-1)^{m'} S_{-m-m'}(n^*,k)(-1)^m. \tag{2.31}$$

This relationship will be incredibly useful in the numerical implementation.

The **Q**-matrix also has some interesting properties. For real potentials, it is Hermitian. This is a direct consequence of the unitarity of the **S**-matrix as

$$\frac{d\mathbf{S}^\dagger\mathbf{S}}{dk} = \frac{d\mathbf{S}^\dagger}{dk}\mathbf{S} + \mathbf{S}^\dagger\frac{d\mathbf{S}}{dk} = 0 \tag{2.32}$$

and

$$\mathbf{Q}^\dagger = i\frac{d\mathbf{S}^\dagger}{dk}\mathbf{S} = -i\mathbf{S}^\dagger\frac{d\mathbf{S}}{dk} = \mathbf{Q} \tag{2.33}$$

The delays associated with the potential are thus always real and the delay eigenstates form a complete basis.

Lorentzian form of the delay.

In the complex case, the phase shifts become complex, as do the time delays. The imaginary part can be interpreted as an emission/absorption time scale.

2.3 Numerical Implementation

The numerical computation of the scattering matrix depends on two constructs: a polar discretization scheme and interior scattering matrices. We choose, for the former, a rather standard radial discretization (see Fig. 2.3). For easier reference, we dub the method the **S**- and **Q**-matrix algorithm (SQA).

The latter relate the solutions of the differential equation inside each radial shell to its neighboring shell. The final interior scattering matrix relates the solution in the last shell to the exterior solution, which is analytically known and is related to the **S**-matrix of the cavity.

Our method is based on an algorithm originally developed by Rahachou and Zozoulenko [20] and extended by [9]. We generalize the method to accept complex refractive index profiles n and wavenumbers k.

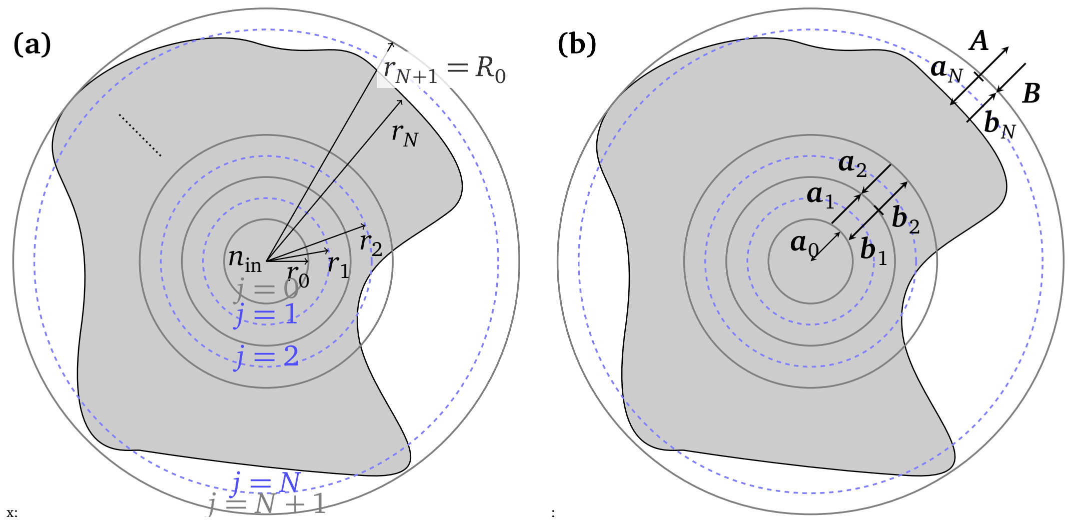

Figure 2.3 – Radial discretization of the cavity for use in SQA. The inner circle is assumed to have a constant refractive index denoted n_{in}. The full grey lines represent the physical boundaries of each shell while the dotted blue lines represent their center.

2.3.1 *Divide et impera*

We wish to solve the Helholtz equation

$$\left[\nabla^2 + k^2 n^2\right]\psi = 0 \tag{2.34}$$

inside the cavity. For $r > R_0$, the radius of the smallest circle that encloses the whole dielectric, the solution is (2.15). We apply the discretization of Fig. 2.3. We define a set of radii $\{r_j\}_{j=0}^{N+1}$ that denote the positions of the center of the different shells. As such, $r_j - r_{j-1} = 2\epsilon$ for the inner shells. The cases $j = 0$ and $j = N + 1$ are different in that r_0 and r_{N+1} denote the outer and inner limits of the domains, respectively. Moreover, $r_{N+1} - r_N = r_1 - r_0 = \epsilon \neq 2\epsilon$. As our first approximation, we suppose that the refractive index inside the inner circle is constant and call it n_{in}. The Helmholtz equation then merely becomes the Bessel equation (A.1). Enforcing finiteness of the field at $r = 0$, we have the solution

$$|\psi(r)\rangle = \sum_m 2a_m^0 J_m(n_{\text{in}} kr) \left|\Phi_m^0\right\rangle \qquad (r < r_0) \tag{2.35}$$

where we have introduced bra-ket notation for the angular part of the solution. In that case,

$$\left\langle \theta \,\middle|\, \Phi_m^0 \right\rangle = e^{im\theta}. \tag{2.36}$$

In the shells $j > 0$, the differential equation to solve is rather

$$\left[\frac{d^2}{dr^2} + \frac{1}{r}\frac{d}{dr} + \frac{1}{r^2}\frac{d^2}{d\theta^2} + k^2 n^2(r,\theta)\right]\psi = 0. \tag{2.37}$$

Inside each shell, we suppose that the potential strength depends only on the angular variable, i.e. $k^2 r^2 n^2(r,\theta) \mapsto k^2 r_j^2 n^2(r_j,\theta)$ such that the angular sampling of the refractive index is done at

$r = r_j$ for each shell. (2.37) is then amenable to a separation of variables

$$\left[\rho_j^2 \frac{d^2}{d\rho_j^2} + \rho_j \frac{d}{d\rho_j} - \xi^j\right] \mathscr{R}^j = 0 \tag{2.38a}$$

$$\left[\frac{d}{d\theta^2} + \left(k^2 n^2(r_j, \theta) r_j^2 + \xi^j\right)\right] \Phi^j = 0 \tag{2.38b}$$

where $\rho_j = r/r_j$ is the scaled radial variable of the shell. These equations can readily be solved by noticing that $\Phi^j(\theta + 2\pi) = \Phi^j(\theta)$. We expand the solution in a Fourier series

$$\left\langle \theta \middle| \Phi_\mu^j \right\rangle = \frac{1}{\sqrt{2\pi}} \sum_{m=-\infty}^{\infty} c_{m\mu}^j e^{im\theta} \tag{2.39}$$

Projecting onto $\left|\Phi_m'^0\right\rangle$ yields

$$\sum_{m=-\infty}^{\infty} \left[-m^2 \left\langle \Phi_{m'}^0 \middle| \Phi_m^j \right\rangle + \xi^j \left\langle \Phi_{m'}^0 \middle| \Phi_m^j \right\rangle + k^2 r_j^2 \left\langle \Phi_{m'}^0 \middle| n^2(r_j, \theta) \middle| \Phi_m^j \right\rangle\right] = 0 \tag{2.40}$$

Noticing that

$$\left\langle \Phi_{m'}^0 \middle| \Phi_m^j \right\rangle = \sum_{m=-\infty}^{\infty} c_{m\mu}^j \delta_{mm'} \tag{2.41}$$

we can write

$$\sum_m \left[-m^2 \delta_{mm'} + \xi^j \delta_{mm'} + \frac{k^2 r_j^2}{2\pi} \int_0^{2\pi} n^2(r, \theta) e^{i(m-m')\theta} d\theta\right] c_{m\mu}^j = 0. \tag{2.42}$$

Using this last equation, we can set up an eigenvalue problem for the separation constant and the Fourier coefficients

$$\mathbf{L}^j \mathbf{c}_\mu^j = \xi_\mu^j \mathbf{c}_\mu^j \tag{2.43}$$

with

$$L_{mm'}^j = m^2 \delta_{mm'} - \frac{k^2 r_j^2}{2\pi} \int_0^{2\pi} n^2(r_j, \theta) e^{i(m-m')\theta} d\theta. \tag{2.44}$$

In the TE case, we must take $n \mapsto n_{\text{eff}}$. This leads us to evaluate the extra integral

$$I = \frac{1}{2\pi} \int_0^{2\pi} \left[\frac{1}{n} \frac{d^2 n(r_j, \theta)}{d\theta^2} - \frac{2}{n^2} \left(\frac{dn(r_j, \theta)}{d\theta}\right)^2\right] e^{i(m-m')\theta} d\theta. \tag{2.45}$$

The numerical cost of this integral can be lessened if we notice that if we write it as a function of n^2 we obtain

$$I = \frac{1}{2\pi} \int_0^{2\pi} \left[\frac{1}{2n^2} \frac{d^2 n^2(r_j, \theta)}{d\theta^2} - \frac{3}{4n^4} \left(\frac{dn^2(r_j, \theta)}{d\theta}\right)^2\right] e^{i(m-m')\theta} d\theta \tag{2.46}$$

which, in turn, can be rewritten as

$$I = \frac{1}{2\pi} \int_0^{2\pi} \left[\frac{1}{2} \frac{d^2 \log n^2(r_j, \theta)}{d\theta^2} - \left(\frac{1}{2} \frac{d \log n^2(r_j, \theta)}{d\theta}\right)^2\right] e^{i(m-m')\theta} d\theta. \tag{2.47}$$

Integrating by parts twice yields

$$I = \frac{1}{2\pi}\int_0^{2\pi}\left[-\frac{(m-m')^2}{2}\log n^2(r_j,\theta) - \left(\frac{1}{2}\frac{d\log n^2(r_j,\theta)}{d\theta}\right)^2\right]e^{i(m-m')\theta}d\theta. \tag{2.48}$$

The second term cannot be integrated out, but this final result means that we will only need to numerically evaluate the first derivative of the refractive index (although its analytical form could be provided).

Notice the form of the $\mathbf{L}^j$ matrix. As can be seem from inspection, the value of the elements depend only on their distance from the diagonal. Taking a closer look reveals the form

$$\mathbf{L}^j = \mathbf{M}^2 + \begin{pmatrix} n_0 & n_{-1} & \cdots & \cdots & n_{-2M} \\ n_1 & n_0 & \cdots & \cdots & n_{-2M-1} \\ n_2 & n_1 & n_0 & \cdots & n_{-2M-2} \\ \vdots & n_2 & n_1 & \ddots & \vdots \\ n_{2M} & \cdots & \cdots & \cdots & n_0 \end{pmatrix} \tag{2.49}$$

which is manifestly Toeplitz. When the potential is real, the Fourier series has the property $n_{-j} = n_j^*$, which makes the $\mathbf{L}^j$ matrix Hermitian. In the general case, however, it is not. Because we will need to use orthogonality relations in what follows, we must compute both the left and right eigenvectors. We will note the left (covariant) basis by $\left|\tilde{\Phi}_\mu^j\right\rangle$. This is not sufficient, however, because we are not guaranteed that both sets of eigenvectors will form a complete basis.

Now that we know the set of eigenvalues $\{\xi_\mu^j\}$, we can solve the radial equation (2.38a). It is instantly recognized as a Cauchy-Euler equation. Given its coefficients, one can write the solution as [21, p. 118-119]

$$\mathscr{R}_\mu^j(r) = a_\mu^j \rho_j^{+\sqrt{\xi_\mu^j}} + b_\mu^j \rho_j^{-\sqrt{\xi_\mu^j}}. \tag{2.50}$$

The solution is now known in all space. We can now apply the boundary conditions (2.12) at the interface of each shell $j \to j+1$. The process generates two sets of equations

$$\sum_\mu \left[a_\mu^j \rho_j^{+\sqrt{\xi_\mu^j}} + b_\mu^j \rho_j^{-\sqrt{\xi_\mu^j}}\right]\left|\Phi_\mu^j\right\rangle = \sum_\mu \left[b_\mu^{j+1}\rho_{j+1}^{+\sqrt{\xi_\mu^{j+1}}} + a_\mu^{j+1}\rho_{j+1}^{-\sqrt{\xi_\mu^{j+1}}}\right]\left|\Phi_\mu^{j+1}\right\rangle \tag{2.51a}$$

$$\eta_j \frac{d}{dr}\sum_\mu \left[a_\mu^j \rho_j^{+\sqrt{\xi_\mu^j}} + b_\mu^j \rho_j^{-\sqrt{\xi_\mu^j}}\right]\left|\Phi_\mu^j\right\rangle = \eta_{j+1}\frac{d}{dr}\sum_\mu \left[b_\mu^{j+1}\rho_{j+1}^{+\sqrt{\xi_\mu^{j+1}}} + b_\mu^{j+1}\rho_{j+1}^{-\sqrt{\xi_\mu^{j+1}}}\right]\left|\Phi_\mu^{j+1}\right\rangle \tag{2.51b}$$

where $\eta_j = 1\,(1/n(r_j,\theta))$ in TM (TE) polarization. The interior scattering matrices are constructed via premultiplying by the left eigenvectors $\left\langle\tilde{\Phi}_\mu^j\right|$ on each side. Combining both resulting equations leads to the linear system

$$\begin{pmatrix} \mathbf{A} & \mathbf{B} \\ \mathbf{C} & \mathbf{D} \end{pmatrix}\begin{pmatrix} \boldsymbol{a}^j \\ \boldsymbol{a}^{j+1} \end{pmatrix} = \begin{pmatrix} \mathbf{E} & \mathbf{F} \\ \mathbf{G} & \mathbf{H} \end{pmatrix}\begin{pmatrix} \boldsymbol{b}^j \\ \boldsymbol{b}^{j+1} \end{pmatrix} \tag{2.52}$$

which can be inverted using Schur's complements to yield a relationship between the $\boldsymbol{a}$ and $\boldsymbol{b}$ coefficients. The matrix relating the four sets of coefficients is an *interior scattering matrix*, $\mathbf{S}^j$. Physically, this relates the locally incoming waves from shell $j+1$ in shell j to the locally outgoing from shell j to shell $j+1$. The last necessary breakthrough is to realize that we can connect the solutions from shell j to those of the shell $j+2$, then $j+3$ and so on. When started from $j=0$, this iterative process yields the relationship

$$\begin{pmatrix} \boldsymbol{a}^0 \\ \boldsymbol{B} \end{pmatrix} = \mathbf{S}^{0,N} \begin{pmatrix} \boldsymbol{a}^0 \\ \boldsymbol{A} \end{pmatrix} \tag{2.53}$$

such that the $\mathbf{S}$-matrix of the system is the block $\mathbf{S}_{22}^{0,N}$. More details can be found in Appendix C.1.

2.3.2 Numerical Analysis and Calibration

While numerical analysis has been heavily formalized in recent years, it is still as much an art as a science. In implementing the algorithm, we thus came across two potential problems: the inversion of the $\mathbf{K}$ matrix (defined below) and the final Hadamard product $\mathscr{H} \circ \mathbf{S}_{22}^{0,N}$. We analyze the two issues and provide solutions to the instability they cause. We also calibrate the method with systems whose analytical solution is known: the homogeneous circular cavity and the annular cavity. We also compare our method to results obtained in the literature.

Numerical Back and Forth

At each step of the algorith, we must invert a matrix of the form

$$\mathbf{K}^{j,j+1} = \left(\frac{r_j - \epsilon}{r_j + \epsilon}\right)^{\mathbf{\Lambda}^j} - \tilde{\mathbf{S}}_{11}^{j+1} \left(\frac{r_j + \epsilon}{r_j - \epsilon}\right)^{\mathbf{\Lambda}^j} \tilde{\mathbf{S}}_{22}^{0,j}. \tag{2.54}$$

Given that the elements of this matrix highly depend upon the discretization parameter ϵ, the half-width of the shells, we can use the condition number W of this matrix as an indicator of the quality of the discretization. It can be grossly estimated by the ratio of the maximum and minimum elements of the matrix. By assuming that there is no amplification in the system, all interior scattering matrices have $||\mathbf{S}|| < 1$ and we can approximate

$$W \sim 1 + \frac{4\lambda_{\max}\epsilon}{r_j}. \tag{2.55}$$

The $\lambda_{\max}$ parameter depends solely on the Fourier components of the refractive index. Given that most cavities that will study will be mildly inhomogenous, i.e. that $|n_0| \geq |n_m|$, we posit the upper bound $|\lambda_{\max}| < 3nkR_0$. A good choice of ϵ is thus

$$\epsilon \ll \frac{1}{12nk} \ll \frac{\lambda}{2n} \tag{2.56}$$

which mirrors the conventional wisdom. This empirical rule is applied in every computation in this thesis.

Introduction to Gerschgorin circles and possibility of inversion problems of $\mathbf{K}$.

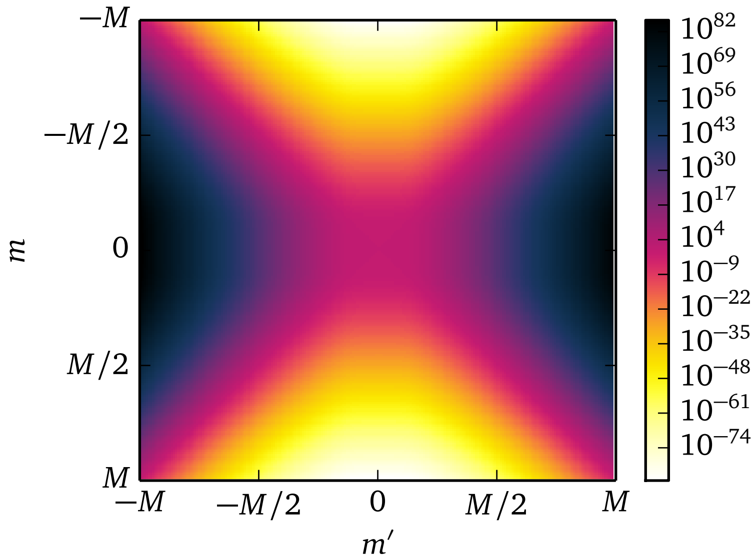

Figure 2.4 – General form of absolute value of the Hankel matrix $\mathscr{H}$. We have used the parameters $z = 10$ and $M = 100$, but the pattern scales with M and z.

Hadamard Product

Like Frodo before Mount Doom, we must face a final challenge before conquering upon all evil, or, in our case, computing the scattering matrix. Our final demon takes the form of the product

$$\mathbf{S} = \left[\mathbf{H}^{(+)}\right]^{-1} \mathbf{S}_{22}^{0,N} \mathbf{H}^{(-)} \tag{2.57}$$

where the $\mathbf{H}$ are diagonal matrices with entries $H_m^{(\pm)}(n_o k R_0)$. We recast the matrix product as a Hadamard (element-wise) product

$$\mathbf{S} = \mathscr{H} \circ \mathbf{S}_{22}^{0,N} \tag{2.58}$$

with $\mathscr{H}_{mm'} = H_m^{(-)}(n_o k R_0)/H_{m'}^{(+)}(n_o k R_0)$. A quick peek at Fig. 2.4 announces the disaster. The region $|m'| > |m|$ increases exponentially with $|m'| - |m|$. This wouldn't be an issue if the corresponding elements of the block scattering matrix $\mathbf{S}_{22}^{0,N}$ were exponentially decreasing (as we physically expect them to); however, the numerical construction of this matrix implies the addition and substraction of $\mathscr{O}(1)$ floating-point numbers, limiting their range to about 10^{-15}, the decimal accuracy associated with `double` precision arithmetic. Consequently, the final Hadamard product yields scattering matrices with unphysically large off-diagonal elements.

Several solutions have been considered, e.g. the use of matrix masks and of higher precision arithmetic. The latter was swiftly abandoned due to the difficulty of the implementation[2], even though it could help stabilize the numerical algorithm [22, §5.8.4]. The use of matrix masks is

[2] Even if we disregard the fact that no C++ compiler support the IEEE 754 `binary128` quadruple precision floating-point representation, we would still need to find numerical libraries that extend the BLAS and LAPACK libraries to work at higher precision.

Show the S-matrix of the quadrupolar cavity

made possible by noting that the cavity cannot convert arbitrarily high angular momenta. The maximum angular momentum it can affect, $M_{\max}$ is a function of its "degree of inhomogeity", characterized by the absolute size of the Fourier components of the refractive index (which also depend on the geometry of the cavity). This gives the **S**-matrix a banded form . The width of this band could be detected in $\mathbf{S}_{22}^{0,N}$ before taking the Hadamard product. After the product, all elements outside this band could be set to zero. The interested reader might want to go through Türeci's discussion of the banded form and the numerical problems associated with the Hankel matrices [23, §3.4].

We have, however, chosen a different path. It turns out that relation (2.31) precisely relates the diverging parts of the Hankel matrix to its vanishing one. Imposing this symmetry on the numerical scattering matrix allows the algorithm to return physical scattering matrices.

Calibration

One of the most important step in algorithmic creation is the *calibration phase*. Ours was calibrated against two cavities: the homogeneous circular cavity and the annular cavity. Their analytical form is given below.

The scattering matrix of the homogeneous circular cavity is trivially obtained. Assuming that the refractive index inside the cavity is n_c and n_o outside, the solution inside the cavity is given by

$$\psi^c = \sum_m a_m^c J_m(n_o kr) e^{im\theta} \tag{2.59}$$

while the solution outside the cavity is given by (2.15). Imposing the electromagnetic boundary conditions yields two infinite sets of equations for three sets of coefficients. Solving yields a linear relationship between the A_m and B_m sets, *viz.* the scattering matrix

$$S_{mm'}^{\mathrm{HD}} = -\frac{\eta_{co} J_m'(Z_c) H_m^{(-)}(Z_o) - J_m(Z_c) H_m^{(-)\prime}(Z_o)}{\eta_{co} J_m'(Z_c) H_m^{(+)}(Z_o) - J_m(Z_c) H_m^{(+)\prime}(Z_o)} \delta_{mm'}. \tag{2.60}$$

where $Z_c = n_c kR_0$, $Z_o = n_o kR_0$ and $\eta_{co} = n_c/n_o$ (n_o/n_c) in TM (TE) polarization.

Calibration with homogeneous circular cavity. Identification of zeroes with peaks of delay matrix. Computation of the zeros in the complex plane.

Derivation of the scattering matrix of the annular cavity is a little more involved. Suffice it to say that it is given by

$$\mathbf{S}^{\mathrm{AC}} = -\left[n_o \mathbf{H}^{(-)\prime}(Z_o) - n_c \mathbf{H}^{(-)}(Z_o)\mathbf{G}\mathbf{F}^{-1}\right]\left[n_o \mathbf{H}^{(+)\prime}(Z_o) - n_c \mathbf{H}^{(+)}(Z_o)\mathbf{G}\mathbf{F}^{-1}\right]^{-1} \tag{2.61}$$

where

$$\mathbf{F} = \mathbf{H}^{(-)}(Z_c) + \mathbf{H}^{(+)}(Z_c)\mathbf{S}^{\mathrm{HD}} \qquad \mathbf{G} = \mathbf{H}^{(-)\prime}(Z_c) + \mathbf{H}^{(+)\prime}(Z_c)\mathbf{S}^{\mathrm{HD}}. \tag{2.62}$$

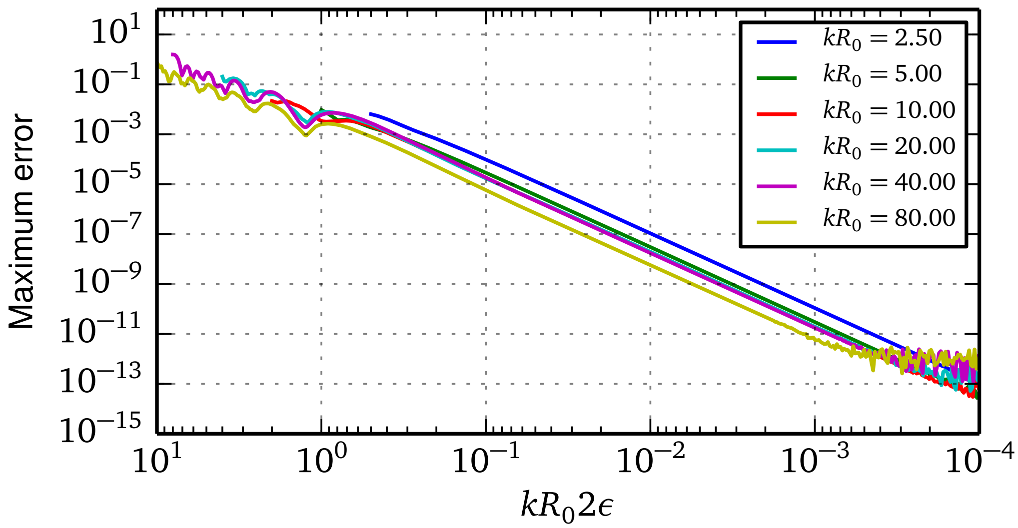

Figure 2.5 – Calibration of SQA against the homogeneous disk. The cavity has refractive index $n_c = 1.5$ and is embedded in air $n_o = 1$. The exterior radius is set to $R_0 = 1$ and we take the number of shells to be $N = 2$. The error approximately follows a cubic power-law behaviour in the discretization size.

A proper derivation can be found in [24]; an improved one can be found in [9, Appendix D].

Calibration with annular cavity.

Comparison with results in the literature.

2.4 Case Study: Gaussian Deformation of the Refractive Index

As an academic demonstration of the power of the method, we present a study of a circular cavity whose refractive index has a Gaussian shape

$$n(r,\theta) = n_0 + \delta n \exp\left[-\frac{r^2 + 2dr\cos(\Theta - \theta) + d^2}{2w^2}\right], \tag{2.63}$$

where n_0 is the background refractive index, δ_n the deformation amplitude, w its half-width and (d, Θ) its position relative to the center of the cavity.

As previously noted by G. P-A. [9], a peculiar duality exists between high-Q resonances and directional emission. Working with a cavity similar to the annular one, it stands to reason that we will recover the same pattern. However, this study will be used as a stepping stone for our inquiries in the realm of non-uniformly pumped active microcavities.

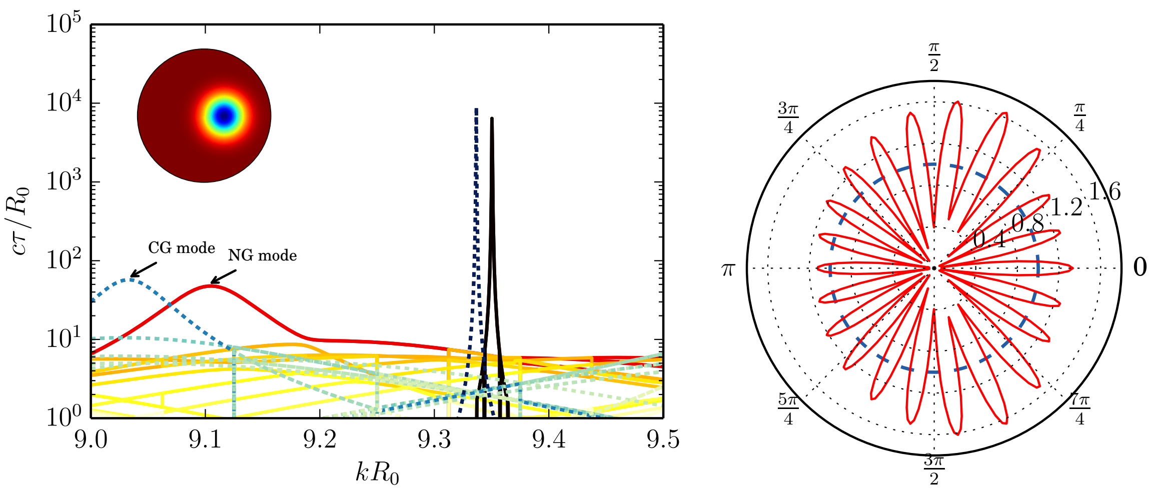

(a) Delay spectrum of the gaussian microcavity.

(b) Far-field

Figure 2.6 – Delay spectrum and far-field.

2.4.1 Loss of Integrability and the KAM Scenario

When $d = 0$, the potential is central and angular momentum is necessarily conserved. If the system is also unitary (no absorption nor gain), it can be shown that the system is integrable[3]. This conservation of angular momentum in turn implies circular symmetry of the fields and hence of the far-field radiation pattern. Since most applications (particularly lasers) require a certain directionality in the emission, our goal is to break the circular symmetry in such a way as to minimize the degradation of the finesse (Q-factor) and maximizing the output directionality. Historically, this goal has spawned the research field of ARCs wherein the boundary of the circular cavity is parametrically deformed to yield limaçon, stadium, elliptical, quadrupolar, etc. shapes.

2.4.2 Numerical Results

2.4.3 Geodesics and Ray Analysis

While our numerical method allows us tu perform full-wave simulations of cavities, it is often useful to consider the associated billiard system, which is the small wavelength approximation of Helmholtz's equation. In homogeneous ARCS, photons follow straight path trajectories and are specularly reflected at the interfaces. In inhomogeneous ARCs, photons follow curved trajectories that obey Fermat's principle. The general equations defining those *geodesic* paths can be found by using the metric

$$(dt)^2 = g_{\mu\nu} dx^{\mu} dx^{\nu}. \tag{2.64}$$

[3] The covariant form of Maxwell's equation and their associated Euler-Lagrange equation make this conservation perfectly clear.

The time it takes to travel a particular trajectory is given by

$$t = \int_{\lambda_0}^{\lambda_1} \sqrt{g_{\mu\nu}\dot{x}^{\mu}\dot{x}^{\nu}}\, d\lambda \tag{2.65}$$

where λ is a parameter of the curve. Applying the Euler-Lagrange equation

$$\frac{\partial L}{\partial x^{\alpha}} - \frac{d}{d\lambda}\frac{\partial L}{\partial \dot{x}^{\alpha}} = 0 \tag{2.66}$$

on the functional $L = \sqrt{w} = \sqrt{g_{\mu\nu}\dot{x}^{\mu}\dot{x}^{\nu}}\, d\lambda$ minimizes the time it takes to travel from one point to another. Evaluating the derivatives

$$\begin{aligned} 0 &= \frac{\partial\left(\sqrt{w}\right)}{\partial x^{\alpha}} - \frac{d}{d\lambda}\frac{\partial\left(\sqrt{w}\right)}{\partial \dot{x}^{\alpha}} \\ &= \frac{\partial w}{\partial x^{\alpha}} + \frac{1}{2\sqrt{w}}\frac{dw}{d\lambda}\frac{\partial w}{\partial \dot{x}^{\alpha}} - \frac{d}{d\lambda}\frac{\partial w}{\partial \dot{x}^{\alpha}} \end{aligned}$$

When λ is an affine parameter, the derivative $dw/d\lambda$ vanishes [25, 26] and the Euler-Lagrange equation becomes

$$\begin{aligned} \frac{\partial w}{\partial x^{\alpha}} &= \frac{d}{d\lambda}\frac{\partial w}{\partial \dot{x}^{\alpha}} \\ g_{\mu\nu,\alpha}\dot{x}^{\mu}\dot{x}^{\nu} &= \frac{d}{d\lambda}\left[g_{\mu\nu}\delta_{\alpha}{}^{\mu}\dot{x}^{\nu} + g_{\mu\nu}\delta_{\alpha}{}^{\nu}\dot{x}^{\mu}\right] \\ &= \frac{d}{d\lambda}\left[g_{\alpha\nu}\dot{x}^{\nu} + g_{\mu\alpha}\dot{x}^{\mu}\right] \\ &= g_{\alpha\nu,\lambda}\dot{x}^{\lambda}\dot{x}^{\nu} + g_{\alpha\nu}\ddot{x}^{\nu} + g_{\mu\alpha,\lambda}\dot{x}^{\lambda}\dot{x}^{\mu} + g_{\mu\alpha}\ddot{x}^{\mu} && \text{(chain rule: } \tfrac{dg_{\mu\nu}}{d\lambda} = \tfrac{\partial g_{\mu\nu}}{\partial x^{\lambda}}\tfrac{dx^{\lambda}}{d\lambda}\text{)} \\ g_{\alpha\nu}\ddot{x}^{\nu} + g_{\mu\alpha}\ddot{x}^{\mu} &= \dot{x}^{\mu}\dot{x}^{\nu}\left[g_{\mu\nu,\alpha} - g_{\alpha\nu,\mu} - g_{\mu\alpha,\nu}\right] && \text{(collecting differentiation orders)} \\ \delta^{\sigma}{}_{\mu}\ddot{x}^{\mu} &= \frac{1}{2}g^{\sigma\alpha}\left[g_{\mu\nu,\alpha} - g_{\alpha\nu,\mu} - g_{\alpha\mu,\nu}\right]\dot{x}^{\mu}\dot{x}^{\nu} && \text{(symmetry of } g_{\mu\nu} \text{ and } \times g^{\sigma\alpha}\text{)} \end{aligned}$$

This finally yields the equation

$$\ddot{x}^{\sigma} + \Gamma^{\sigma}{}_{\mu\nu}\dot{x}^{\mu}\dot{x}^{\nu} = 0 \tag{2.67}$$

where $\Gamma^{\sigma}{}_{\mu\nu}$ are the Christoffel symbols of the second kind.

Discuss the results.

Discuss the geodesics in this geometry.

2.5 Perspectives

Optimization of refractive index profile and geometry for specific purposes.

Optmization of pump profile, refractive index profile and geometry for specific purposes.

Use of integral methods to numerically solve scattering problem (may load to more stable algorithms).

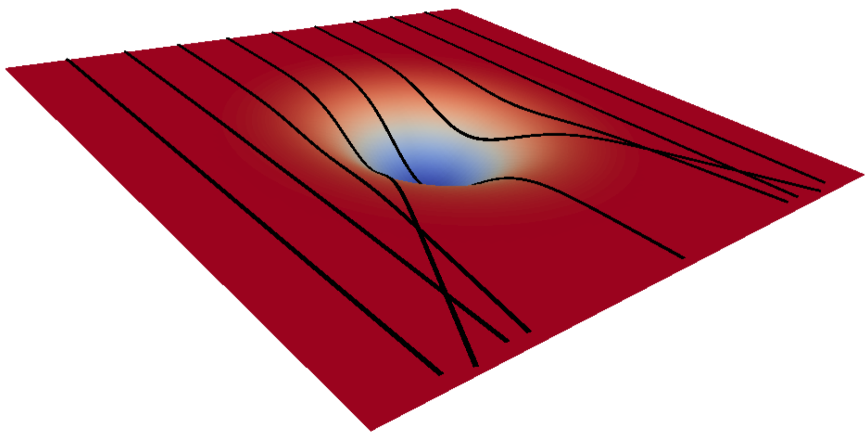

Figure 2.7 – Trajectories for photons of different impact parameters. The trajectories are the geodesics of the relevant "optical spacetime", where the curvature of space represents the optical distance that the photon has to traverse. The central region, where the refractive index is lower, acts as a diverging lens.

Chapter 3

Active Media and Radiation

3.1 Lasing and Scattering

3.1.1 Modeling the Quantum Gain Medium

Primer on SALT and its derivation for TM/TE modes.

3.1.2 Variable Phase Method

Primer on VPM for bidimensional cavities (mention its use for 3D cavities with vector spherical wave functions).

Motivation for VPM: computing the field more efficiently than in SQA.

3.2 Antenna Propagation

Describe goal of project; advantages of using fibers over patch antennae...

3.2.1 Antenna Theory Primer

Basic definitions of directivity, gain...

Stratton solution

3.2.2 Designs

Feasability of design via dipole antenna. Analytical solution of dipole antenna. Issue with thin silver shells.

Theory of infinite LCXs as guide for finite LCX. Discuss in more detail about the thin silver shells (methods used to model them, non-agreement with experimental data and its probable causes). Discuss Bruggemann's model and Fuchs-Sondheimer methods.

Chapter 4

Conclusion

Appendix A

Bessel Functions

This appendix contains some results concerning the Bessel functions. Given our redution of Maxwell's equations from 3D to 2D using cylindrical coordinates, the Bessel functions will form the basis of our analysis, as the Bessel functions are the eigenfunctions of Helmholtz's equation in those coordinates.

We thus wish to collect some of their most important properties here for easy reference. Most of them come from the celebrated volume by Abromowitz & Stegun [27], while a few come from [28]. Proper reference will be given.

In what follows, $\nu, z \in \mathbb{C}$ and $n \in \mathbb{N}$ unless explicitly stated otherwise.

A.1 Definition and Elementary Properties

A.1.1 Differential Equation

The Bessel functions solve the differential equation

$$z^2 \frac{d^2 w}{dz^2} + z \frac{dw}{dz} + (z^2 - \nu^2) w = 0 \tag{A.1}$$

which is a special case of the confluent hypergeometric differential equation, which is in turn a special case of the hypergeometric differential equation. When solved via Fröbenius' method, it yields the solution

$$J_\nu(z) = \sum_{k=0}^{\infty} \frac{(-1)^k \left(\frac{1}{2}z\right)^{\nu+2k}}{k!\Gamma(\nu+k+1)}. \tag{A.2}$$

This is the Bessel function of the first kind. A second, linearly independant is defined by

$$Y_\nu(z) = \frac{J_\nu(z)\cos\pi\nu - J_{-\nu}(z)}{\sin\pi\nu} \tag{A.3}$$

where a valid limiting process must be used when $\nu \to n$.

We will be mostly interested in a second set of linearly independant solutions: the Hankel functions. They are defined by

$$H_\nu^{(+)}(z) = J_\nu(z) + iY_\nu(z) \tag{A.4a}$$
$$H_\nu^{(-)}(z) = J_\nu(z) - iY_\nu(z). \tag{A.4b}$$

We will alternatively use the notation

$$H_\nu^{(\omega)} = J_\nu(z) + i\omega Y_\nu(z) \qquad (\omega = \pm) \tag{A.5}$$

to describe both functions at the same time.

A.1.2 Recurrence Relations

From the differential equation itself, we can derive multiple recurrence relations that the whole family of Bessel functions obey. If $\mathscr{C}$ denotes J, Y, $H^{(\pm)}$ or any linear combination of the four functions, we have

$$\mathscr{C}_{\nu-1}(z) + \mathscr{C}_{\nu+1}(z) = \frac{2\nu}{z}\mathscr{C}_\nu(z) \tag{A.6a}$$
$$\mathscr{C}_{\nu-1}(z) - \mathscr{C}_{\nu+1}(z) = 2\mathscr{C}_\nu'(z) \tag{A.6b}$$
$$\mathscr{C}_{\nu-1}(z) - \frac{\nu}{z}\mathscr{C}_\nu(z) = \mathscr{C}_\nu'(z) \tag{A.6c}$$
$$-\mathscr{C}_{\nu+1}(z) + \frac{\nu}{z}\mathscr{C}_\nu(z) = \mathscr{C}_\nu'(z). \tag{A.6d}$$

However, the minimal solution to these recurrence relations is $J_\nu(z)$, so any attempt at numerically evaluating Y or $H_\nu^{(\pm)}$ using these is foiled (see §C.2 for details).

A.1.3 Relations between Solutions

The following are analytical relationships between the set of Bessel functions. They can be of use in both standard and numerical analysis.

Reflection Formulas [29, p. 286]

$$J_{-\nu}(z) = \cos\nu\pi J_\nu(z) - \sin\nu\pi Y_\nu(z) \tag{A.7a}$$
$$Y_{-\nu}(z) = \sin\nu\pi J_\nu(z) + \cos\nu\pi Y_\nu(z) \tag{A.7b}$$
$$J_{-n}(z) = (-1)^n J_n(z) \tag{A.7c}$$
$$Y_{-n}(z) = (-1)^n Y_n(z) \tag{A.7d}$$
$$H_{-\nu}^{(\omega)} = e^{i\omega\nu\pi} H_\nu^{(\omega)} \tag{A.7e}$$

Complex Conjugate ($\nu \in \mathbb{R}$)

$$\overline{J_\nu(z)} = J_\nu(\overline{z}) \tag{A.8a}$$

$$\overline{Y_\nu(z)} = Y_\nu(\overline{z}) \tag{A.8b}$$

$$\overline{H_\nu^{\omega}(z)} = H_\nu^{(-\omega)}(\overline{z}) \tag{A.8c}$$

A.2 Asymptotic and Limiting Forms

A.2.1 Expansions for Small Arguments and Fixed ν

From the first few terms of the power series (A.1),

$$J_\nu(z) = \frac{1}{\Gamma(\nu+1)}\left(\frac{z}{2}\right)^\nu\left[1 - \frac{1}{\nu+1}\left(\frac{z}{2}\right)^2\right] + \mathcal{O}(z^{\nu+4}). \tag{A.9}$$

Using the first terms of the ascending series [27, §9.1.11]

$$\begin{aligned} Y_n(z) = -\frac{1}{\pi}\left(\frac{z}{2}\right)^{-n}\sum_{k=0}^{n-1}\frac{(n-k-1)!}{k!}\left(\frac{z}{2}\right)^{2k} + \frac{2}{\pi}\ln\frac{z}{2}J_n(z) \\ -\frac{1}{\pi}\left(\frac{z}{2}\right)^n\sum_{k=0}^{\infty}\{\psi(k+1)+\psi(n+k+1)\}\left(\frac{z}{2}\right)^{2k}\frac{1}{k!(n+k)!}, \end{aligned} \tag{A.10}$$

where

$$\psi(n+1) = -\gamma + \sum_{k=1}^{n} k^{-1} \qquad (\gamma = 0.57721\,56649\ldots) \tag{A.11}$$

is the digamma function. The cases $n = 0$ and $n \neq 0$ differ

$$Y_0(z) = \frac{2}{\pi}\left(\ln\frac{z}{2} + \gamma\right) + \mathcal{O}(z^2) \tag{A.12}$$

$$Y_n(z) = -\frac{(n-1)!}{\pi}\left(\frac{z}{2}\right)^{-n} + \mathcal{O}(z^{-n+2}). \tag{A.13}$$

The expansions of the Hankel functions is found by using their definition (A.4):

$$H_0^{(\omega)}(z) = 1 + \frac{2i\omega}{\pi}\left(\ln\frac{z}{2} + \gamma\right) + \mathcal{O}(z^2) \tag{A.14}$$

$$H_n^{(\omega)}(z) = -\frac{i\omega(m-1)!}{\pi}\left(\frac{z}{2}\right)^{-n} + \mathcal{O}(z^{-n+2}). \tag{A.15}$$

A.2.2 Expansions for Large Arguments and Fixed ν

The Bessel functions, jealous of the simpler trigonometric functions, try to mimic them when their arguments get large. We have

$$J_\nu(z) \approx \sqrt{\frac{2}{\pi z}} \cos\left(z - \frac{\nu\pi}{2} - \frac{\pi}{4}\right) \tag{A.16a}$$

$$Y_\nu(z) \approx \sqrt{\frac{2}{\pi z}} \sin\left(z - \frac{\nu\pi}{2} - \frac{\pi}{4}\right) \tag{A.16b}$$

$$H_\nu^{(\omega)}(z) \approx \sqrt{\frac{2}{\pi z}} e^{i\omega\left(z - \frac{\nu\pi}{2} - \frac{\pi}{4}\right)} \tag{A.16c}$$

Appendix B

Basic Equations of Bidimensional Cavities

B.1 SALT Equations for TE and TM Polarizations

B.2 Specialization to Dielecric Cavities

Appendix C

Numerical Tools

C.1 Numerical Computation of the Scattering Matrix

C.2 Computation of the Logarithmic Derivative $[H_\nu^{(\pm)}(z)]'/H_\nu^{(\pm)}(z)$

As we have seen from Appendix B, the computation of the logarithmic derivative of Bessel functions is of the upmost importance in the numerical solution of scattering problems. Given that we already use Amos' library to evaluate the Bessel functions, we might have been tempted to use it to directly evaluate the derivative. It turns out that using expansions that pertain to logarithmic derivatives is somewhat faster and is more accurate than using Amos' library.

In this section, we introduce some concepts relating to continued fraction expansions (CFEs) and discuss their numerical evaluation. We then derive the CFEs and other expansions that will be of use in the computation of the logarithmic derivatives.

C.2.1 Notation and Necessary Theorems

A continued fraction expansion is a representation of a mathemetical function. It can be linked to Laurent series, Padé approximants and much more [28]. It has the standard form

$$f = b_0 + \cfrac{a_1}{b_1 + \cfrac{a_2}{b_2 + \cfrac{a_3}{b_3 + \cfrac{a_4}{b_4 + \cdots}}}} \tag{C.1}$$

or, more succinctly,

$$f = b_0 + \operatorname*{K}_{m=1}^{\infty}\left(\frac{a_m}{b_m}\right) \tag{C.2}$$

where 'K' is for the German word *Kettenbruch*, meaning continued fraction. We define the nth approximant as

$$f_n = b_0 + \operatorname*{K}_{m=1}^{n}\left(\frac{a_m}{b_m}\right). \tag{C.3}$$

We will be concerned with their numerical evaluation and convergence properties.

Notice that naïvely evaluating the CFE from right-to-left, as a person would do, does not yield a satisfying numerical algorithm, as the amount of iterations must be fixed in advance and consequently does not allow the control the accuracy of the evaluation. The chosen method is taken from the Holy Bible of Numerics, *Numerical Recipes* [29] and is called the modified Lentz's method. It constructs a rational approximation of the nth approximant

$$f_n = \frac{A_n}{B_n} \tag{C.4}$$

where

$$\begin{aligned} A_{-1} &= 1 & B_{-1} &= 0 \\ A_0 &= b_0 & B_0 &= 1 \\ A_j &= b_j A_{j-1} + a_j A_{j-2} & B_j &= b_j B_{j-1} + a_j B_{j-2}. \end{aligned} \tag{C.5}$$

This method can lead to over/underflow of the floating-point representation: the method hence uses

$$\begin{aligned} C_j &= A_j/A_{j-1} & D_j &= B_{j-1}/B_j \\ &= b_j + \frac{a_j}{C_{j-1}} & &= \frac{1}{b_j + a_j D_{j-1}} \\ f_j &= f_{j-1}C_j D_j. \end{aligned} \tag{C.6}$$

The method is aptly described by Algorithm 1. It allows for a left-to-right evaluation of the CFE and control of the relative accuracy of the computation.

As for the convergence properties, we will only bother with CFEs originating from three-term recurrence relations. Indeed, it turns out that any three-term recurrence relation can be linked to a CFE. Consider

$$y_{n+1} + a_n y_n + b_n y_{n-1} = 0. \tag{C.7}$$

It can be rewritten as

$$\frac{y_n}{y_{n-1}} = -\frac{b_n}{a_n + y_{n+1}/y_n}. \tag{C.8}$$

Iterating yields the CFE

$$\frac{y_n}{y_{n-1}} = \operatorname*{K}_{m=n}^{\infty}\left(\frac{-b_m}{a_m}\right). \tag{C.9}$$

Given our goal of computing $[H_\nu^{(\pm)}(z)]'/H_\nu^{(\pm)}(z)$ and in light of (ref to recurrence relation of Bessel functions), it seems that we have won. The next theorem, however, will prove us wrong.

Algorithm 1: Evaluation of Continued Fractions

Data: `tiny` = square root of smallest representable number
Data: `eps` = accuracy of the CFE
if $b_0 = 0$ **then**
  $f_0 \leftarrow$`tiny`
else
  $f_0 \leftarrow 0$
$C_0 \leftarrow f_0$;
$D_0 \leftarrow 0$;
repeat from $j = 1$
  $D_j \leftarrow b_j + a_j D_{j-1}$;
  if $D_j = 0$ **then**
    $D_j \leftarrow$`tiny`
  $C_j \leftarrow b_j + \frac{a_j}{C_{j-1}}$;
  if $C_j = 0$ **then**
    $C_j \leftarrow$`tiny`
  $D_j \leftarrow 1/D_j$;
  $\Delta_j \leftarrow C_j D_j$;
  $f_j \leftarrow f_{j-1}\Delta_j$
until $|\Delta_j - 1| <$`eps`;
return f_j

Theorem C.1 (Pincherle's Theorem [28]). *If there exists a minimal solution u_n of the three-term recurrence relation* (C.7)*, the associated CFE* (C.9) *converges to u_n/u_{n-1}. A solution is said minimal if there exists another solution v_n such that*

$$\lim_{n\to\infty} \frac{u_n}{v_n} = 0. \tag{C.10}$$

v_n is said to be the dominant solution. The minimal solution is unique.

Because the minimal solution of (A.6a) if $J_\nu(z)$, we cannot use the associated CFE to compute the logarithmic derivatives of Hankel functions. Instead, we must look into the links between Hankel functions and confluent hypergeometric functions.

C.2.2 CFE and Other Expansions

In this brief foray into the vast subject of hypergeometric functions, we will introduce Kummer's function and its link to the evaluation of the logarithmic derivative.

Kummer's function solves the differential equation [27, §13.1.1]

$$z\frac{d^2y}{dz^2} + (b-z)\frac{dy}{dz} - ay = 0 \tag{C.11}$$

and is noted $U(a,b,z)$. It can be shown that that $u_k = (a)_k U(a+k,b,z)$ is the minimal solution of the recurrence [30]

$$u_{n+1} = \frac{2a-b+2n+z}{a-b+n+1} u_n - \frac{a+n-1}{a-b+n+1} u_{n-1} \tag{C.12}$$

where $(a)_k$ is the Pochhammer symbol. We can hence derive

$$\frac{U(a,b,z)}{U(a+1,b,z)} = 2a-b+2+z - \operatorname*{K}_{m=1}^{\infty}\left(\frac{(a+m)(b-a-m-1)}{b-2a-2m-2-z}\right). \tag{C.13}$$

Combined with [27, §13.4.23]

$$U(a+1,b,z) = \frac{1}{1+a-b} U(a,b,z) + \frac{z}{a(1+a-b)} U'(a,b,z), \tag{C.14}$$

we obtain [28]

$$\frac{dU(a,b,z)/dz}{U(a,b,z)} = -\frac{a}{z} + \frac{a(1+a-b)/z}{2a-b+2+z\,-} \operatorname*{K}_{m=1}^{\infty}\left(\frac{(a+m)(b-a-m-1)}{b-2a-2m-2-z}\right). \tag{C.15}$$

Given the relation between Kummer's functions and Hankel functions $H_\nu^\omega(z)$ [27, §13.6.22/23]

$$H_\nu^\omega(z) = \frac{2}{\sqrt{\pi}} e^{-\omega[\pi(\nu+1/2)-z]} (2z)^\nu U(\nu+1/2, 2\nu+1, -2i\omega z) \qquad (\omega = \pm) \tag{C.16}$$

we can finally find the CFE

$$\frac{dH_\nu^\omega(z)/dz}{H_\nu^\omega(z)} = -\frac{1}{2z} + i\omega + \frac{\omega}{z} \operatorname*{K}_{m=1}^{\infty}\left(\frac{\nu^2-(2m-1)^2/4}{2(iz-\omega m)}\right). \tag{C.17}$$

In our numerical implementation (see next section), we have found that when $|z| < 10^{-2}$, convergence is slow. This mirrors the results of [31]. We thus use the small argument expansions for the Bessel functions (*q.v.* §A.2.1) to obtain

$$\lim_{z\to 0} \frac{dH_\nu^\omega(z)/dz}{H_\nu^\omega(z)} = -\frac{\nu}{z} \qquad (\nu \neq 0) \tag{C.18a}$$

$$= \frac{1}{z}\left[\frac{\pi}{2i\omega} + \gamma + \ln\left(\frac{z}{2}\right)\right]^{-1} \qquad (\nu = 0). \tag{C.18b}$$

C.2.3 Numerical Tests

We have performed a number of tests to ascertain the performance of our algorithm. To test the precision of the algorithm, we have evaluated the CFE for $z \in \{0, 10\}$ and $\nu \in \{-100, 100\} \in \mathbb{N}$ and compared it to the values obtained via Amos' library for a range of tolerances. It can be seen that the maximum deviation decreases until our set tolerance hits 10^{-12} and then plateaus. Because convergence of C.17 is mathematically insured, we conclude that Amos's library evaluate the logarithmic derivative up to a precision of 10^{-12}. This is probably due to the propagation of errors in the floating point operations, as we use relation (A.6b) to evaluate the derivative.

However, it can be seen that Amos' library is somewhat faster, given its precision, that our CFE evaluation even though it requires three Hankel function evaluations.

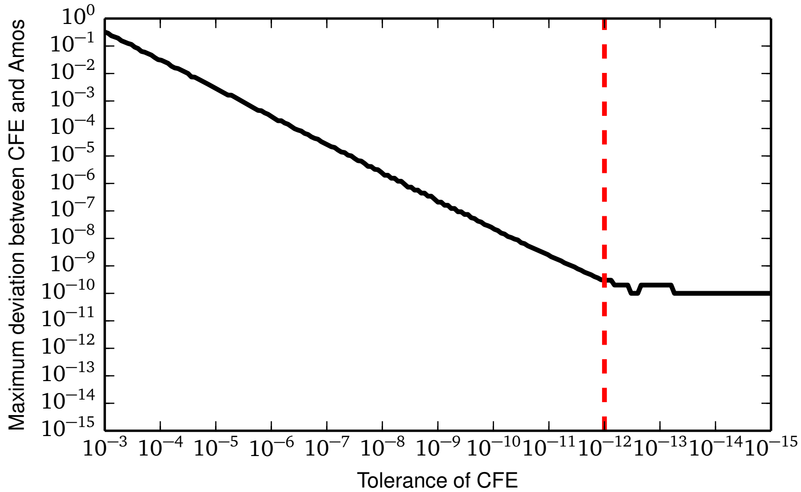

Figure C.1 – Maximum deviation between the CFE and Amos' implementation of the Bessel functions as a function of the tolerance of the CFE. This study was performed in the parameter space $z \in \{0.1, 10\}$, $\nu \in \{-100, 100\}$. We interpret the plateau in maximum deviation as the error committed by Amos' implementation, i.e. Amos' implementation has a precision of $\sim 10^{-10}$ on the evaluation of the logarithmic derivative.

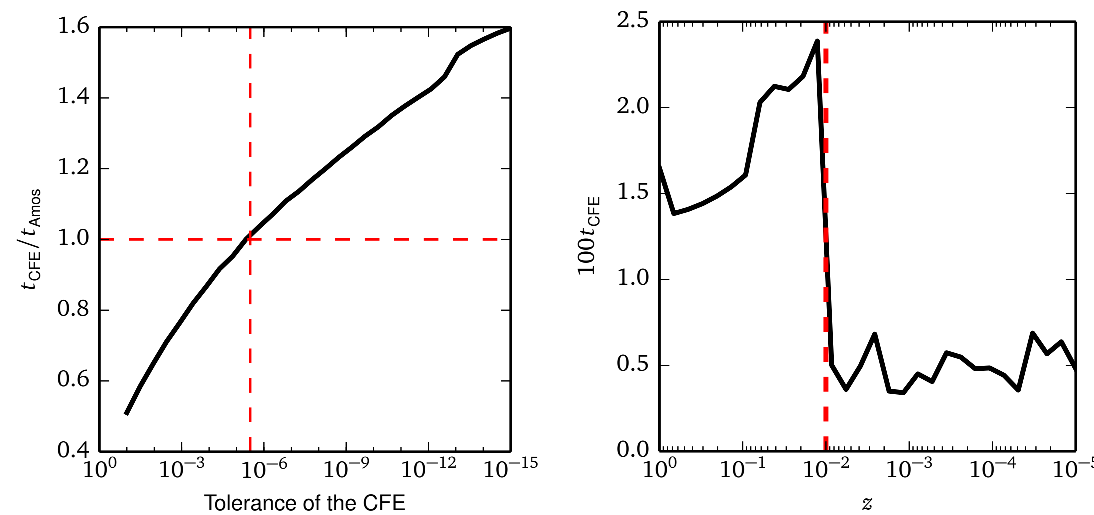

(a) Performance of the CFE implementation as a function of its tolerance. We measured the ratio of the time it takes to compute the logarithmic derivative at $z = 0$ for all orders $\nu \in \{-100, 100\}$ with the CFE and Amos' implementation. When the tolerance of the CFE hits $\sim 10^{-5.5}$, the CFE is slower than Amos' implementation.

(b) Performance of the CFE as a function of z. When approaching $z = 0$ (from all sides), it takes a higher number of terms for the CFE to converge, resulting in a slower algorithm. However, at $z = 10^{-2}$, we use the small argument form, preserving both precision and performance.

Figure C.2 – Performance of the CFE compared to that of Amos' library. The CFE is somewhat slower, but can achieve better precision.

C.3 Clebsch-Gordan Coefficients and Wigner Symbols

Bibliography

[1] J. W. Strutt (Lord Rayleigh), *Theory of Sound*, vol. II (MacMillan, London, 1878).

[2] J. W. Strutt (Lord Rayleigh), “The Problem of the Whispering Gallagery,” Philos. Mag. **20**, 1001–1004 (1910).

[3] O. Wright, “Gallery of whispers,” Phys. World pp. 31–36 (2012).

[4] Y. Yamamoto and R. E. Slusher, “Optical Processes in Microcavities,” Phys. Today **46**, 66 (1993).

[5] A. Serpengüzel, S. Arnold, and G. Griffel, “Excitation of resonances of microspheres on an optical fiber,” Opt. Lett. **20**, 654–656 (1995).

[6] F. Vollmer, D. Braun, A. Libchaber, M. Khoshsima, I. Teraoka, and S. Arnold, “Protein detection by optical shift of a resonant microcavity,” Appl. Phys. Lett. **80**, 4057 (2002).

[7] D. K. Armani, T. J. Kippenberg, S. M. Spillane, and K. J. Vahala, “Ultra-high-Q toroid microcavity on a chip,” Nature **421**, 925–8 (2003).

[8] F. Vollmer and S. Arnold, “Whispering-gallery-mode biosensing: label-free detection down to single molecules,” Nat. Methods **5**, 591–596 (2008).

[9] G. Painchaud-April, “Dielectric Cavities: Scattering Formalism and Applications,” Ph. d. thesis, Université Laval.

[10] J. D. Jackson, *Classical Electrodynamics* (John Wiley & Sons, 1962).

[11] H. G. L. Schwefel, “Directionality and Vector Resonances of Regular and Chaotic Dielectric Microcavities,” Ph. d. thesis, Yale University (2004).

[12] R. Dubertrand, E. Bogomolny, N. Djellali, M. Lebental, and C. Schmit, “Circular dielectric cavity and its deformations,” Phys. Rev. A **77**, 013804 (2008).

[13] S. Bittner, E. Bogomolny, B. Dietz, M. Miski-Oglu, P. Oria Iriarte, A. Richter, and F. Schäfer, “Experimental test of a trace formula for two-dimensional dielectric resonators,” Phys. Rev. E **81**, 066215 (2010).

[14] C. P. Dettmann, G. V. Morozov, M. Sieber, and H. Waalkens, "Unidirectional emission from circular dielectric microresonators with a point scatterer," Phys. Rev. A **80**, 063813 (2009).

[15] J. A. Stratton, *Electromagnetic Theory* (McGraw-Hill Book Company, 1941).

[16] F. T. Smith, "Lifetime Matrix in Collision Theory," Phys. Rev. **118**, 349–356 (1960).

[17] L. Eisenbud, "The Formal Properties of Nuclear Collisions," Ph. d., Princeton University (1948).

[18] C. A. A. de Carvalho and H. M. Nussenzveig, "Time delay," Phys. Rep. **364**, 83–174 (2002).

[19] R. G. Newton, *Scattering Theory of Waves and Particles* (Springer-Verlag, New York, 1982), 2nd ed.

[20] A. I. Rahachou and I. V. Zozoulenko, "Scattering Matrix Approach to the Resonant States and Q Values of Microdisk Lasing Cavities," Appl. Opt. **43**, 1761–1772 (2004).

[21] M. Greenberg, *Advanced Engineering Mathematics* (Pearson, 1998).

[22] M. I. Mishchenko, L. D. Travis, and A. A. Lacis, *Scattering, Absorption and Emission of Light by Small Particles* (Cambridge University Press, 2002), 3rd ed.

[23] H. E. Türeci, "Wave Chaos in Dielectric Resonators : Asymptotic and Numerical Approaches," Ph. d. thesis, Yale University (2003).

[24] M. Hentschel and K. Richter, "Quantum chaos in optical systems: The annular billiard," Phys. Rev. E **66**, 056207 (2002).

[25] V. A. Toponogov, *Differential Geometry of Curves and Surfaces: A Concise Guide* (Birkhäuser, 2005), 1st ed.

[26] B. Schutz, *A First Course in General Relativity* (Cambridge University Press, 2009), 2nd ed.

[27] M. Abramowitz and I. A. Stegun, *Handbook of Mathematical Functions* (Dover Publications, 1965).

[28] A. Cuyt, V. B. Petersen, B. Verdonk, H. Waadeland, and W. B. Jones, *Handbook of Continued Fractions for Special Functions* (Springer, 2008).

[29] W. H. Press, S. A. Teukolsky, W. T. Vetterling, and B. P. Flannery, *Numerical Recipes : the Art of Scientific Computing* (Cambridge University Press, 2007), 3rd ed.

[30] N. M. Temme, "The numerical computation of the confluent hypergeometric function U(a, b, z)," Numer. Math. **41**, 63–82 (1983).

[31] I. Thompson and A. Barnett, "Coulomb and Bessel functions of complex arguments and order," J. Comput. Phys. **64**, 490–509 (1986).

Index

Glossary

calibration phase (of an algorithm) Wherein a numerical algorithm is tested against a problem with aknown solution. Oftentimes, convergence properties of the algorithm are determined using this (usually) trivial scenario.. 20

Q-matrix Time-delay matrix. 5, 9, 13, 14

S-matrix Scattering matrix. 3, 5, 11, 14, 18, 20

Acronyms

ARC asymmetric resonant cavity. 3, 22

FEM finite element method. 4

LCX leaky coax antenna. 4

SALT steady-state *ab initio* laser theory. 4

SQA the **S**- and **Q**-matrix algorithm. 14, 15, 21